An analysis of future malaria intensity and climatic suitability in Uganda.

Assessing spatial variation, temporal variation and uncertainty in the projected malaria transmission season

Tom Hartgers

5920639

Applied Data Science

First supervisor: Prof. dr. Derek Karssenberg

Second supervisor: Dr. Menno Straatsma

Utrecht University

Abstract

Malaria is a large health threat on the African continent. The transmission of the parasite is highly dependent on precipitation and temperature levels. Relatively low temperatures in the highlands of Uganda can be inhibiting the current spread of malaria. Future climate change may therefore cause a shift in the climatic suitability for malaria transmission in this region. This study uses downscaled climate projections of temperature and precipitation values in Uganda from 2015 to 2099 generated by the MPI-ESM1-2-LR climate model. This data is used as input for a simplified version of the Liverpool Malaria Model. The model mathematically simulates several processes of the malaria transmission dynamics on a daily basis for every grid cell of the input data. The output consists of the daily basic reproductive rate (R_0). The rate serves as a measure for the climatic suitability for and intensity of malaria transmission. Error margins for the climate projections are estimated through an ensemble created on a spatial subset of Uganda and are combined with the input data. The malaria model uncertainty is assessed through a sensitivity analysis using a one-at-a-time (OAT) method. Results show an increase in areas where, on average, malaria will spread ($R_0 > 1$). This is most notable under climate change scenarios SSP3-7.0 (up to 24.1% of the area) and SSP 5-8.5 (up to 34.7% of the area). Several high-altitude locations in the west and east of Uganda show higher R_0 values ($R_0 \geq 2.5$) starting from 2050. This is mainly caused by high levels of projected precipitation in the aforementioned scenarios. These locations also display the most notable increase in malaria transmission season length from 80 up to 120 days per year. The moment in time the season occurs appears stable. The error analysis warrants caution regarding the interpretation of these results, showing high errors for precipitation at high-altitude locations. Furthermore, the sensitivity analysis indicates a model that is highly sensitive to its parameter settings. Additional research needs to be carried out to calibrate the model parameters and to validate the outcomes of the current contribution.

Table of contents

1. Introduction

Malaria has been an ever-present health threat in the continent of Africa. In sub-Saharan Africa there have been 228 million cases and 405,000 deaths in 2018 alone (Mordecai et al., 2020). The way that malaria is transmitted, is dependent on several factors. These factors, biotic or abiotic in nature, include precipitation and temperature levels. They partially determine within which geographical reach the disease can occur and spread. Due to anthropogenic global warming and climate change, these factors can become subject to change. Therefore, it can be expected that the spatial distribution of Malaria will change as well (Eikenberry and Gumel, 2018).

Multiple models have been proposed to simulate the spatial and temporal distribution of malaria (Eikenberry and Gumel, 2018). One of these models is the Liverpool Malaria Model (LMM), developed by Hoshen and Morse (2004). It attempts to simulate the parasite and vector dynamics, using inputs of daily rainfall and daily temperatures. The output consists of malaria incidence for a region, as well as other intermediate statistics, such as the size of the mosquito population (Hoshen and Morse, 2004). The model has in later stages been simplified by Jones (2007) to output the basic reproduction number (R_0). This model, the LMM_R0 model, does not directly relate back to the population that is at risk of malaria. Instead, it can give an indication of the climatic suitability for and intensity of malaria transmission; if R_0 is larger than one, malaria will spread. By doing so it can delineate, for example, the start and end of the malaria transmission seasons (Caminade et al., 2014).

Recent developments in climate modelling have enabled researchers to feed the malaria models output from climate projection models. One of these developments is the sixth phase of the Coupled Models Intercomparison Project (CMIP6) (Eyring et al., 2016). CMIP6 has enabled researchers to distribute, compare and access different climate model outputs. Thereby it helps create a deeper understanding of the effects of climate change. The output of CMIP6 has improved compared to its predecessor CMIP5. These improvements include better projections of mean and extreme climate and more reliable results (for a comprehensive overview of research focussing on CMIP6 improvements see Ayugi et al., 2021). Several models that are gathered in CMIP6 have subsequently been downscaled by the Climate Impact Lab (CIL), resulting in a dataset containing daily maximum and minimum temperatures and precipitation values (Gergel et al., 2023; Gergel et al., 2022).

These projections can be used to analyse the changing temperatures and rainfall of regions that are exposed to the threat of malaria. Combining this data with malaria models can indicate whether a region will be susceptible to an increased or decreased risk of malaria. The highlands of East Africa are considered to be an area that can become exposed to an increased risk of malaria. In this region the malaria burden was previously rare but has become more prevalent since the 1970s (Eikenberry and Gumel, 2018). In this region the spread can be contained by the low temperatures at high altitudes. Rising temperatures could create a more suitable climate for malaria to spread (Hay et al., 2002). Additionally, malaria reproduction is heavily dependent on the availability of freshwater pools (Hoshen and Morse, 2004) and the East African highlands is susceptible to biannual, seasonal rainfalls. These span from March to May (MAM) and October to December (OND). This could therefore, combined with rising temperatures, result in two highly suitable periods for malaria transmission (Palmer et al., 2023).

This study will investigate the current outlook of the projected risk of malaria for a specific case in the East African highlands: Uganda. The climatic suitability for and intensity of malaria under four different climate scenarios will be analysed using the downscaled data from the Climate Impact Lab. The data will serve as input for the LMM_R0 model, which calculates the daily basic reproduction number (R_0) for a time period from 2015 to 2100. The central research question is: How does the climatic suitability for and intensity of malaria change under different climate change scenarios in Uganda between 2015 and 2100, and what degree of uncertainty can be associated with these projections? To answer this question we will answer the following questions and subquestions:

1. How will the spatial and temporal variation of precipitation and temperature in Uganda change, according to the different climate change scenarios?

2. How does the spatial distribution of areas where, on average, $R_0 > 1$ change over time, according to different climate change scenarios?

3. How will the temporal and spatial variation of the malaria transmission season length per climate scenario in Uganda change over time?
   a. Is there a difference in trend of the malaria transmission season length between the biannual rainy seasons?

4. Will the moment when the malaria transmission season occurs shift forward or backward in the two respective rainy seasons?

5. How do error measures in climate projections and model output vary in terms of their spatial and temporal distribution?

6. How sensitive is the LMM_R0 model to different parameter settings?

The climate model that will be used for this analysis is the MPI-ESM1-2-LR model (MPI model) (Wieners et al., 2019a; Wieners et al., 2019b), which has shown adequate results for both temperature and precipitation forecasting in East Africa (Ayugi et al., 2021a, 2021b). Data is available for four different climate scenarios that are further elaborated upon in the data section of this paper. Assessment of temperature and precipitation trends will be carried out with this dataset. The changes in malaria intensity and climatic suitability will be studied by calculating daily R_0 values through the LMM_R0 model. Python code for the model is accessible through the IBM Github repository of Kuehnert (2022) and has subsequently been adapted to work with the xarray dataformat.

The alterations in the spatial distribution of areas suitable for malaria transmission will be assessed by averaging R_0 over three 20-year time frames. The changing season lengths will be measured by the periods where R_0 is larger than one. These values are compared over the years but also between the biannual rainy seasons. The moment in time of the transmission season will be assessed by calculating the average day-of-season count where $R_0 > 1$. This will indicate where on average in the biannual season the malaria transmission season occurs.

The uncertainty of the MPI model will be assessed by creating an ensemble of climate projections from models that have shown adequate performance in predicting temperature and precipitation in Uganda. This ensemble will be created for a spatial subset of Uganda, covering an area of 1° x 1°. The standard deviation of the precipitation and temperature values between models will be calculated for each datapoint and averaged over the two spatial dimensions, resulting in a variable error band that can be added to the MPI climate projections as a minimum and maximum value at each timestep. The spatial distribution of these errors will also be assessed. Daily temperature and precipitation error values will be averaged over time and plotted for three different time frames. Additionally, the spatial distribution of R_0 error values will be determined by calculating them for all possible combinations of precipitation and temperature data, sourced from the different models that were gathered in the respective ensembles. Finally, the sensitivity of the model parameters will be assessed by running the model for a range of possible parameter values. Through a

one-at-a-time (OAT) analysis, all parameter values will be fixed apart from one. By doing so, R_0 can be determined for a range of parameter settings. The average R_0 values and input values per parameter will be plotted against each other to visualise the sensitivity of the model for every parameter.

The report is structured as follows. First, a description of the datasets will be given, highlighting their origin and how they have been pre-processed. Secondly, in the methodology chapter, the report will elaborate on the biological malaria system and how it relates to the calculations in the LMM_R0 model. Further methods for measuring and comparing the malaria seasons will also be elaborated upon. Thirdly, the results will be presented. Fourthly, the results will be discussed, after which the report will arrive at its final conclusion.

2. Data

2.1. Data description

To estimate R0, this study uses data that is collected as part of the CMIP6 project, which was started by the World Climate Research Programme (WCRP). The project, currently in phase 6, is one of the foundations of climate research (Eyring et al., 2016). A multitude of different global circulation models (GCM) are combined under its umbrella. Several of these models have been downscaled by the Climate Impact Lab (CIL), providing daily temperature and precipitation projections. From these models, the dataset from the MPI model has been selected as the main model for this study (Wieners et al., 2019a; Wieners et al., 2019b). The model, which was run by the Max Planck Institute for Meteorology in Hamburg, has shown adequate performance for predicting both temperature and precipitation values in East Africa (Ayugi et al., 2021a, 2021b). Additionally, the CMIP5 version of the model has been used in another study to forecast malaria trends in the Lake Victoria basin, which is part of our study region (Ototo et al., 2022). The CIL downscaled the output of this model using the Quantile Delta Mapping (QDM) bias-adjustment method. Thereby they preserved trends in the distribution tails of the data (Gergel et al., 2023). Bias correction and downscaling was done through the historical ERA5 dataset (Hersbach et al., 2020; Sabater, 2019; Sabater, 2021).
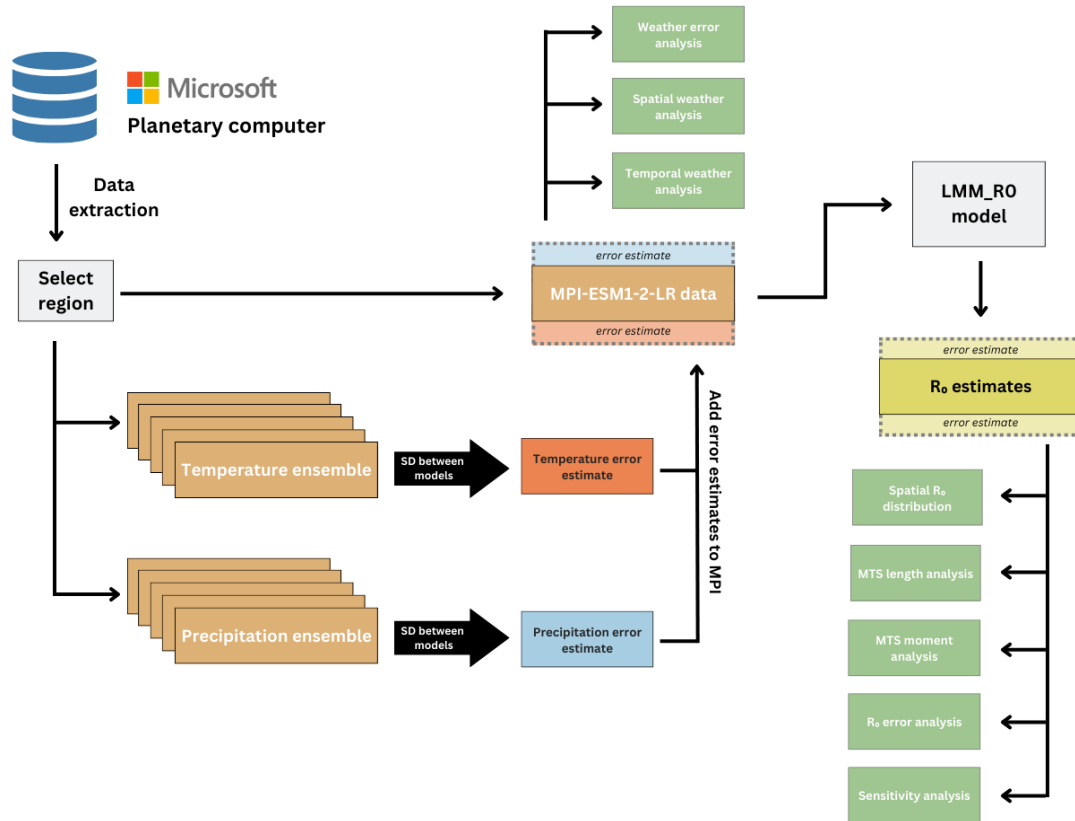
Figure 1: Overview of data, workflow and methods used for analysis. MTS: Malaria transmission season, SD: Standard deviation

The data is accessible on the planetary computer from Microsoft (*Microsoft Planetary Computer*, n.d.). Access to the data is provided through the Planetary Computer STAC API, that facilitates the import of the data to Python in the xarray dataformat, creating structured and labelled multi-dimensional arrays. The data includes historical data, as well as projections for different climate trajectories as established in the AR6 synthesis report of the Intergovernmental Panel on Climate Change (IPCC, 2023a). The scenarios are defined by different Shared Socioeconomic Pathways (SSPs) ranging from aggressive mitigation to no mitigation of harmful effects on the climate: SSP1-2.6, SSP2-4.5, SSP3-7.0, and SSP5-8.5 (Riahi et al., 2017). The temperature changes associated with these scenarios are further elaborated upon in Table 1. The scenarios are named according to a template: SSP*x-y*. *X* refers to the SSP that describes the socioeconomic trends that underpin the different scenarios. *Y* refers to the level of radiative forcing resulting from the respective SSP in the year 2100. This is expressed in watts per square metre (IPCC, 2023a). It should be noted that scenario SSP5-8.5 has become less likely according to the IPCC. It can however not be ruled out, as the relative temperature rise can also occur from lower emission scenarios (IPCC, 2023b).

Category description (likelihood)	GHG emissions scenario
Limit warming to 2°C (>67%)	Low (SSP1-2.6)
Limit warming to 3°C (>50%)	Intermediate (SSP2-4.5)
Limit warming to 4°C (>50%)	High (SSP3-7.0)
Exceed warming of 4°C (>50%)	Very high (SSP5-8.5)

Table 1:Description of scenarios and modelled pathways considered across the AR6 Working Group reports of the IPCC. The description column denotes to what extent the global rise in temperature is mitigated. The right column shows which greenhouse gases (GHG) scenarios are associated with respective temperature rise. Values from IPCC (2023a).

The dimensions of the array with its extent and resolutions are described in Table 2.

Dimension	Extent	Resolution
Time - Historical	01/01/1950 - 12/31/2014	Daily
Time - SSP projections	01/01/2015 - 12/31/2100	Daily
Latitude	-90° to 90°	0.25° grid cells
Longitude	-180° to 180°	0.25° grid cells

Table 2: Dimensions of the dataset with their extent and resolution.

The dataset contains three variables across the aforementioned dimensions. The minimum and maximum temperature (variables: *tasmin* and *tasmax*) are provided in Kelvin (K) and daily cumulative surface precipitation values are provided in mm day^{-1} (variable: *pr*).

Next to the main model, several other models have been selected to create ensembles for an uncertainty estimation. These models were selected based on their availability within the planetary computer, the number of climate scenarios covered by the model and their performance regarding rainfall and temperature projections in Uganda and East Africa. For each variable (temperature and precipitation) five models were selected to create an ensemble. Table 3 shows an overview of which models were selected with references to the

literature that formed the basis for selection and references to the origin of the model. All models have the same dimensions and extent as presented in Table 2.

Variable	Model	Selection reference	Origin reference
Precipitation	GFDL-ESM4	Ngoma et al. (2021a)	Krasting et al. (2018); John et al. (2018)
	CanESM5	Ngoma et al. (2021a)	Swart et al. (2019a); Swart et al. (2019b)
	NorESM2-MM	Ngoma et al. (2021a)	Bentsen et al. (2019a); Bentsen et al. (2019b)
	UKESM1-0-LL	Ngoma et al. (2021a)	Good et al. (2019); Tang et al. (2019)
	MPI-ESM1-2-LR	Ayugi et al., (2021b)	Wieners et al. (2019a); Wieners et al. (2019b)
Temperature	FGOALS-g3	Ayugi et al. (2021)	Li (2019); Li (2019b)
	MPI-ESM1-2-LR	Ayugi et al. (2021)	Wieners et al. (2019a); Wieners et al. (2019b)
	EC-Earth3	Babaousmail et al. (2023)	EC-Earth (2019a); EC-Earth(2019b)
	BCC-CSM2-MR	Babaousmail et al. (2023)	Xin et al. (2018); Xin et al. (2019)
	EC-Earth3-veg	Babaousmail et al. (2023)	EC-Earth(2019c); EC-Earth(2019d)

Table 3: Ensemble models per variable including reference to papers where the selection was based on and the references to the original models.

2.2. Data preparation

2.2.1. MPI model data preparation

The data from the MPI model was imported to a Python environment using the xarray library. Uganda was selected through a bounding box that was made up of the coordinates in Table 4. The topography of Uganda is shown in Figure 2.

Area	Lon	Lat
Uganda	29° E - 35° E	2° S - 4.7°N
Ensemble area	30° E - 31° E	1° S - 0°

Table 4: Coordinates of the bounding box used to select Uganda
and the study region of the ensemble.

After selecting the area of Uganda, the data is further processed. The minimum and maximum temperature values are converted to degrees Celsius by subtracting 273.15 from the Kelvin units. The model requires daily average temperatures as input. These values are however not directly available. Instead, the daily max temperature, offset by -5°C, will be used, as was done in the original LMM (Hoshen and Morse, 2004). Therefore, five degrees were subtracted from the maximum temperature values. Then, for every day the mean precipitation of the previous ten days is calculated through a rolling window function xarray. This will be used to calculate the new daily influx of mosquitoes. Lastly every year is divided into two seasons: a spring season and a fall season. The seasons last from January 1 to June 30 and from July 1st to December 31st respectively. This split ensures that the biannual rainfalls (periods MAM and OND) occur in the middle of the season. When seasons are mentioned in this report, they will refer to these periods. The malaria transmission season (MTS) will refer to the period when the climate is suitable for malaria transmission ($R_0 > 1$).

The 20 largest urban centres of Uganda were plotted on the R_0 and MTS length maps to illustrate if and how the changing risk of malaria could affect these locations. The cities along with their coordinates and population counts, based on a census conducted in 2014 by the Uganda Bureau of Statistics, can be found in appendix A. It shows that 4,168,128 out of 34,634,650, around 12% of the population of Uganda, lived in the twenty largest urban centres in 2014 (Uganda Bureau of Statistics, 2016).
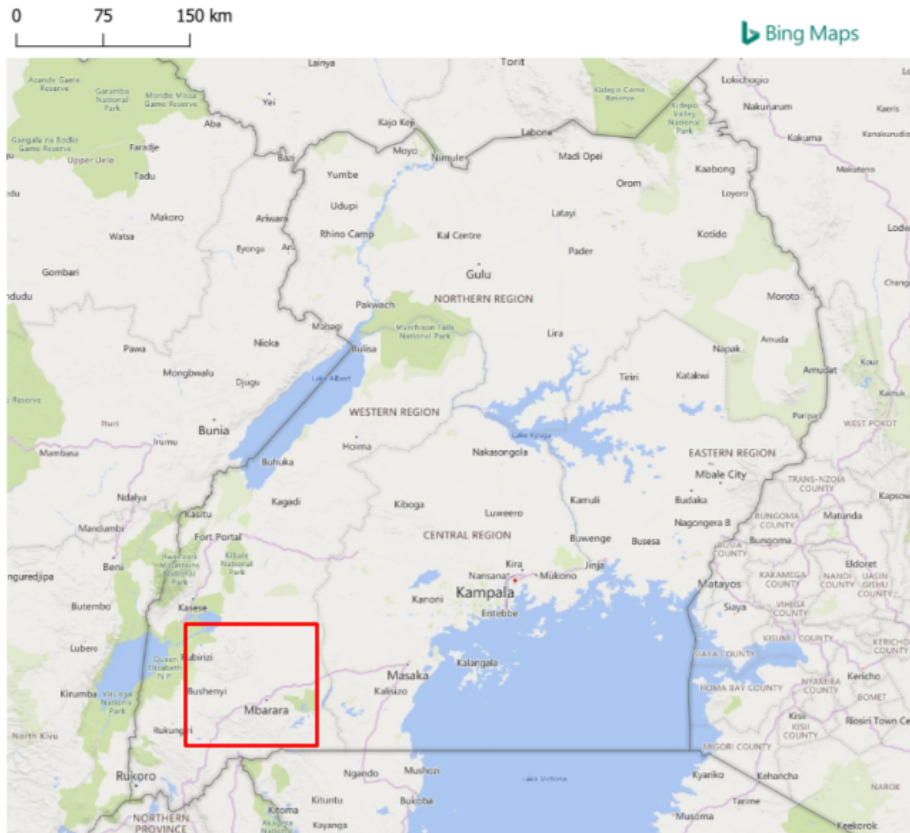
Figure 2: Uganda topography and major cities (© 2023 Microsoft). The red delineated area shows the spatial subset used for ensemble creation.

2.2.1 Ensemble data preparation

Due to computational limitations it was not possible to create an ensemble of 5 models for the full extent of Uganda that spanned the entire timespan of the projections. Therefore, a 1° x 1° spatial subset was selected. An area with a relative high degree of variation in altitude was selected to compensate for the loss of spatial variation. The selected area is delineated by the red box in Figure 2 and by the coordinates in Table 4.

3. Methodology

3.1 The LMM_R0 model and the malaria life cycle

To assess climatic suitability changes of the study region, this study will make use of the LMM_R0 model from Jones (2007). The model uses input of rainfall and temperature to calculate the basic reproduction rate (R_0) for every day. To do so the model is run forward in time on a raster dataset that contains daily temperature and precipitation values. It will be run on the raster dataset that was described above, with a 0.25° x 0.25° spatial resolution,

containing daily values from 01-01-2015 to 31-12-2100. The model is a local model and therefore does not simulate spatial interactions between grid cells.

In order to better understand the LMM_R0 model, a basic understanding of the malaria system is required. The lifecycle of the malaria parasite and its vector host is a complex phenomenon. Simply stated, malaria is caused by a parasite known as *Plasmodium* that can infect human blood cells and reproduce in them. Once these parasites get consumed by a susceptible vector host (in this case a female *Anopheles* mosquito) through a blood meal, the parasite develops within the vector host. After this development, the vector host can infect new human hosts by transferring the parasite to the new host through a blood meal. These blood meals are taken by mosquitoes to grow eggs and thereby sustain the mosquito population (Eikenberry & Gumel, 2018). All these processes are relevant when modelling the spread of malaria. Figure 3 shows the most important aspects of malaria transmission as modelled in the original Liverpool Malaria Model (Hoshen and Morse, 2004). An elaboration on the different cycles and how they relate back to the LMM_R0 model can be found in the subsections below.
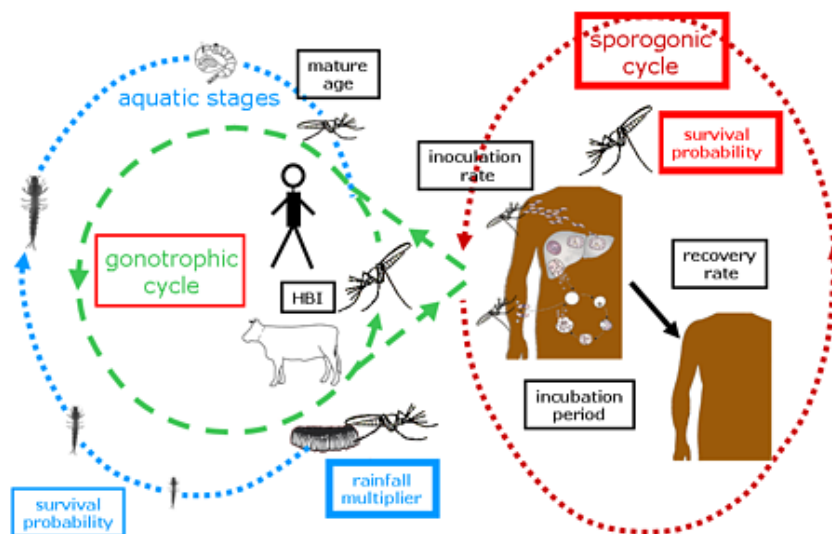
Figure 3: Components of the Liverpool Malaria Model (Malaris, n.d.)

3.1.1. The gonotrophic cycle

The gonotrophic cycle is concerned with the development of eggs within the vector host. When fully developed, these eggs are deposited into suitable breeding areas (freshwater pools), where the larvae can further develop. The egg development is highly temperature dependent. To quantify the combination of temperature and time, a degree-day dependence

was detected by Detinova (1962). Detinova concluded that the cycle for egg development lasts 37 days above a temperature threshold T_g. Egg development will halt when the temperature is below this threshold. The formula to calculate the length of the gonotrophic cycle in days, dependent on temperature can be expressed as:

$$G_{days,\,t} = 1 + \frac{D_g}{T_t - T_g} \tag{1}$$

where D_g is the amount of degree days necessary for development, T_t the temperature at day t in °C, T_g the threshold temperature in °C beneath which the development halts and $G_{days,\,t}$ the length of the gonotrophic cycle in days at day t. In the tropics, the value of $G_{days,\,t}$ lies around 3 days.

3.1.2. The sporogonic cycle

When a vector host has taken a blood meal from an infected person, then this mosquito will become infected with a certain probability. This is called the inoculation efficiency for mosquitoes and is represented in the model by parameter c. Once the parasite is inside the mosquito midgut, sporogony occurs, leading to the development of parasitic forms that are infectious to humans (Antinori et al., 2012). Again the progress of the sporogonic cycle is degree-day dependent. The cycle lasts 111 degree-days above a threshold of 18°C (Detinova, 1962). The length of the cycle in days can be expressed as follows:

$$S_{days,\,t} = 1 + \frac{D_s}{T_t - T_s} \tag{2}$$

where D_s is the amount of degree days necessary for development, T_t the temperature at day t in °C, T_s the threshold temperature in °C beneath which the development halts (18°C in this case) and $G_{days,\,t}$ the length of the gonotrophic cycle in days at day t.

3.1.3. Mosquito population dynamics

The mosquito population survives every day with a probability P to the next day. This probability is heavily dependent on temperature. To describe this relation, several mosquito survival schemes have been proposed based on past experiments (Ermert et al., 2011). The survival probability scheme used in this paper is based on the work of Martens (1998) and follows the following distribution:

$$P_t = 0.45 + 0.054 \cdot T_t - 0.0016 \cdot T_t^2 \tag{3}$$

Where P_t is the survival probability at day t, and T_t the temperature in °C at day t. The probability can be multiplied by the mosquito population per day to determine the amount of surviving mosquitoes to the next day. The relationship between temperature and the survival probability has been visualised in Figure 4.
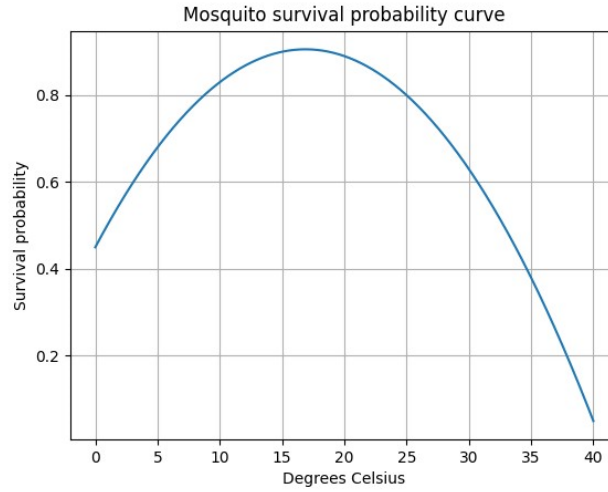

Figure 4: Mosquito survival probability as a function of temperature according to Martens (1998) (authors image).

New mosquitoes enter the population when eggs have matured to larvae and pupae. These eggs were oviposited into freshwater pools and therefore the development of new, immature mosquitoes is highly dependent on the existence of water bodies (Hoshen and Morse, 2004). This availability of pools is simulated in the LMM_R0 model by computing the average rainfall over the previous ten days:

$$mos_t = mos_{t-1} \cdot P_{t-1} + R_{mult} \cdot R_d + R_{offset} \tag{4}$$

where mos_t is the mosquito population at timestep t and P_{t-1} the mosquito survival probability of the previous day. R_{mult} is the rainfall multiplier that determines how many mosquitoes are added proportional to the rainfall. R_d is the average daily rainfall of the previous ten days and R_{offset} is the rainfall offset. In this case the model assumes a linear relationship between rainfall and new adult mosquitoes that enter the population.

3.1.4. Calculating R_0

The output of the model will be the basic reproduction rate R_0. The basic reproduction rate is the average number of newly infected cases that is produced by one infectious case. In the case of malaria, an infected case refers to an infected human host. The rate can give an indication of when an outbreak can occur and its intensity. When R_0 is larger than 1, the disease will spread. If R_0 is smaller than one, the disease will likely die out (Smith et al., 2007). Before calculating R_0 the LMM_R0 model requires additional parameters.

Firstly it requires the human blood index (*HBI*). The human blood index is a fixed parameter that indicates the preference of mosquitoes to bite humans over cattle. This preference is used to calculate the human biting rate, that denotes the number of bites on humans made by a single mosquito per day:

$$a_t = \frac{HBI}{G_{days,\,t}} \tag{5}$$

where a_t is the human biting rate at timestep t, and $G_{days,\,t}$ the length of the gonotrophic cycle in days at timestep t. Then, the adult mosquito mortality (μ) is calculated. This denotes the mosquito mortality rate for every timestep:

$$\mu_t = -1 \cdot log(P_t) \tag{6}$$

where μ_t is the adult mosquito mortality at timestep t and P_t the survival probability at timestep t.

This enables the model to calculate the transmission potential. This can serve as an index of malaria risk. If the transmission potential is high, then fewer mosquitoes are required for the disease to spread (Jones, 2007). It is calculated as follows:

$$TP_t = \frac{a_t^2 \cdot b \cdot c \cdot exp(-\mu_t \cdot S_{days,\,t} - r \cdot HIA)}{\mu_t \cdot r} \tag{7}$$

where TP_t is the transmission potential at timestep t. Next to variables that have been calculated in previous steps, other fixed parameters are used to calculate the *TP*. The inoculation efficiency for humans and for mosquitoes is respectively represented by

parameter *b* and *c*. Inoculation efficiency denotes the probability that a susceptible human or mosquito is infected with the parasite after an infectious bite. The human recovery rate is represented by *r*. This rate denotes how quickly infected individuals clear an infection and become susceptible again. This parameter is set at 0.0284, enabling 90% of the infected population to become susceptible again after 80 days (Ermert et al., 2011).

Finally the transmission potential is multiplied by the mosquito population, resulting in R_0:

$$R_{0,t} = mos_t \cdot TP_t \tag{8}$$

A full list of the parameters and their values can be found in appendix B. The calculations are repeated in appendix C.

3.2. Quantifying changes in climatic suitability

3.2.1. Meteorological changes

An analysis of the temperature and precipitation values will illustrate how the weather in Uganda will change under different climate scenarios according to the MPI climate model. For every climate scenario the mean of the daily precipitation and temperatures are calculated per year and plotted over time. Additionally, the spatial distribution will be assessed by firstly calculating the mean spatial distribution of the daily values for the time frame from 2015 to 2020. Then, the change in precipitation and temperature will be plotted with respect to the time frames 2040-2060 and 2080-2099. By doing so, the changes in the spatial distribution of weather can be assessed for different time frames.

3.2.2. Average spatial distribution of R_0

The spatial distribution of R_0 will be assessed in a similar way as the meteorological changes from section 3.2.1.. The average R_0 values will be plotted on the map of Uganda for three time frames: 2020-2040, 2050-2070 and 2080-2099. This will give an indication of how the spatial distribution of areas where the average $R_0 > 1$ will change in the future. To quantify these differences, the proportion of the study area where $R_0 > 1$ will also be calculated and reported for every time frame.

3.2.3. MTS length

The MTS length will be examined by evaluating how many days per year $R_0 > 1$. To smooth out daily error, the rolling five-day average of R_0 will be taken, creating a more stable estimate. Then, per season (spring and fall), the number of days with $R_0 > 1$ will be calculated. The temporal trend in MTS length per season will be assessed by plotting the spatial mean over time per scenario (including the error analysis). The average spatial variation will be assessed by plotting the temporal mean of three twenty-year periods (2020-2040, 2050-2070, 2080-2100) per scenario on a map of the area.

3.2.4. MTS moment in season

The occurrence, or the moment in the season when, on average, $R_0 > 1$ will be utilised to determine if there is a shift in the average timing of the MTS within the biannual seasons. To do so, the day-of-year counts (0 to 365) will be split up into two seasons. The day-of-year count will be reset at the half year mark, creating a day-of-season count for the two seasons. The days per year and season where $R_0 > 1$ will be registered and averaged. This will result in the average moment in time of the MTS for that season. These values will be spatially averaged for each season, creating two MTS moments per year (one for the fall season and one for the spring season). These values will be plotted over time to analyse a possible shift in when the MTS occurs in the season.

3.2.5. Error analysis

The uncertainty in the projections of temperature and precipitation will be assessed next to the meteorological changes. This will be done through an analysis of an ensemble of different climate models. The ensemble is created for each variable (temperature and precipitation) and for each scenario from the models in Table 3. The error should reflect the variation in the outcomes of the different, yet equally probable climate scenarios (Woldemeskel et al., 2012). Therefore, the standard deviation between models will be calculated for each datapoint. This will capture the variance in observations between models. Then, the standard deviations will be averaged over the two spatial dimensions. This will result in a dataset of standard deviations per timestep, per SSP scenario and per variable that can be analysed over time.

The spatial error distribution will be calculated by averaging the precipitation and temperature standard deviations over time for three time frames: 2020-2040, 2050-2070 and

2080-2099. Different combinations of ensembles will also be used to assess the spatial distribution of the error of the R_0 estimates. There are 25 possible combinations between the temperature and precipitation models that were selected for the ensemble (Table 3). Every combination will serve as input for temperature and precipitation values in the LMM_R0 model. The standard deviations of R_0 will then be computed across these 25 iterations and averaged over time for three time frames: 2020-2040, 2050-2070 and 2080-2099.

3.2.6. Sensitivity analysis

A sensitivity analysis will be conducted to assess how the different parameters of the model can affect the model output. The parameter settings used by Kuehnert (2022) will be the default settings of the model. The possible ranges of the parameters are specified for most parameters in Jones (2007). The values for the rainfall offset parameter, human inoculation efficiency (*b*) and the mosquito inoculation efficiency (*c*) were not specified by Jones. To still test parameter sensitivity, custom ranges were adapted. All parameter ranges can be found in the parameter table of appendix B.

For each parameter a list of ten equally spaced values within this range will be generated. The default settings of the model will be maintained for all parameters, apart from the parameter under investigation. For every value per parameter, the R_0 values from 2015 to 2099 will be calculated for a single gridcell. This gridcell will be selected to have an average R_0 of around 1, to ensure that the values can fluctuate up and down. This point is located at 1.125°N and 34.12°E for SSP1-2.6. All values will be averaged over time, resulting in one R_0 value per parameter setting. The R_0 values will be plotted against the different input values to visualise the sensitivity of the model to each parameter.

4. Results

4.1. Meteorological changes

4.1.1. Precipitation

The changes in the average daily precipitation in the projections of the MPI model per year have been plotted in Figure 6. To address the uncertainty in the precipitation forecasts, the values from the error analysis for every timestep have been added and subtracted from the MPI values to create the error bands. The trends in error values are presented in section 4.1.3.. The precipitation values show some variation around the 5 mm per day mark for all

scenarios. A larger degree of uncertainty can be observed in the SSP3-7.0 and SSP5-8.5 scenarios. The error bands become larger after 2075 with respect to the other two SSP scenarios.
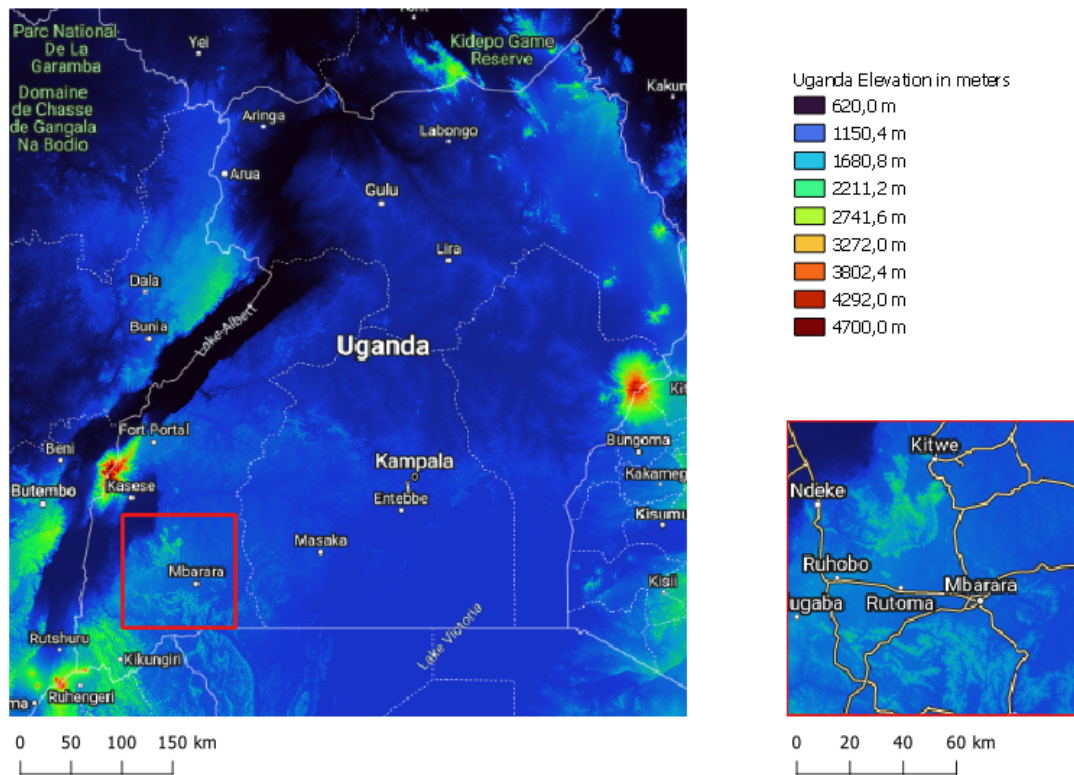

Figure 5: Uganda elevation map (European Space Agency, 2021) and major cities (Map data ©2015 Google).. Left panel shows the study region. Right panel shows the red highlighted area that was used for ensemble creation.
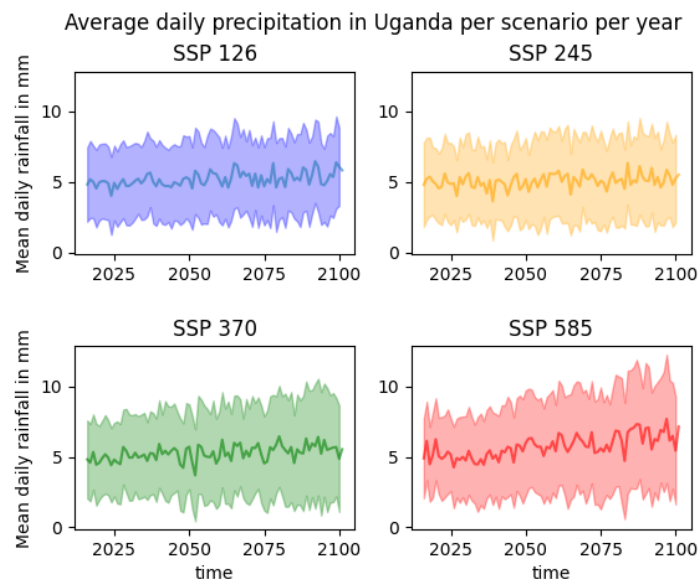

Figure 6: average daily precipitation in mm per year. Daily precipitation values were averaged over the two spatial dimensions and resampled to a yearly mean. The lighter coloured error bands as calculated in section 4.5.1. have been added around the line of our main model

The spatial distribution of the changes in mean daily precipitation values have been plotted in Figure 7. Precipitation values are highest in the southwest of the country from 2015 to 2020. This corresponds to high-altitude locations in Uganda(see Figure 5). This pattern can be observed across all four scenarios. The changes throughout the timeframes (6B: 2040-2060 and 6C: 2080-2099) don't exclusively show the same distribution. For scenarios SSP3-7.0 and SSP5-8.5 a similar distribution can be shown in the difference in precipitation; it mainly increases where the precipitation hotspots occur. The average daily precipitation in these two scenarios exhibits an increase of up to 5 or 6 mm, corresponding to a 20% rise. SSP1-2.6 and SSP2-4.5 show only little increase or decrease in the amount of precipitation.
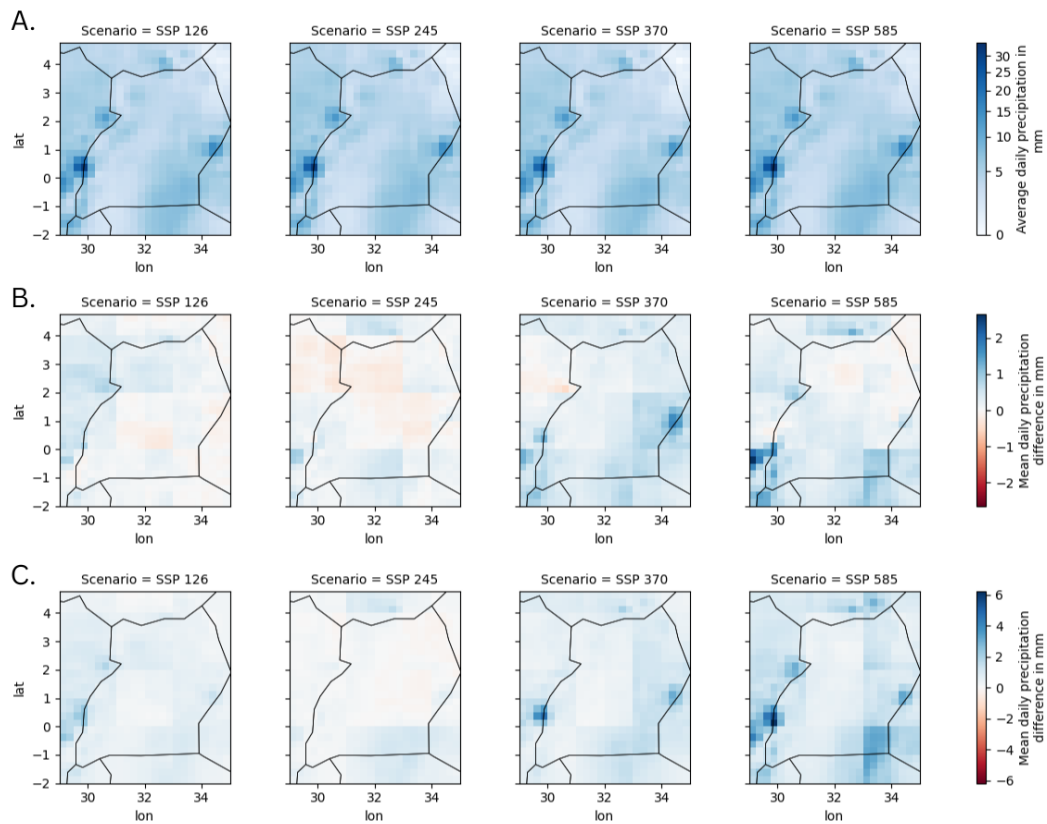

Figure 7: Average daily precipitation over Uganda from 2015-2022 in mm per day (A) and the changes with respect to A. for the average daily precipitation of time frames 2040-2060 (B) and 2080-2099 (C) in mm per day. Note that figure A has been plotted on a power scale where gamma = 0.5

4.1.2. Temperature

The temperature projections of the MPI model have been plotted in Figure 8. To account for temperature forecast uncertainty, error bands were created by adding and subtracting values from the error analysis for each timestep to the MPI. A positive trend can be detected in scenarios SSP2-4.5, SSP3-7.0 and SSP5-8.5. Especially the latter two show a clear upward trend in temperature. Scenario SSP1-2.6 shows a fluctuating but rather stable line around the 23°C mark.

The spatial distribution of the mean daily temperature between 2015 and 2020 has been plotted in Figure 9A. The difference between these values and the mean daily temperatures from 2040 to 2060 and 2080 to 2099 have been plotted in Figure 9B and 9C respectively. Temperatures are higher in the north of the country for all scenarios from 2015 to 2020. Temperatures rise for all scenarios in Figure 9B, with notable increases observed in SSP2.4-5 and SSP5-8.5, reaching a maximum of 1°C. In Figure 9C the temperature increase becomes larger for all scenarios. For SSP5-8.5 this increase becomes more pronounced up to around 2.5°C. The spatial focus of the temperature rises differs per scenario and per plotted timeframe. Figure 9B shows a focus in the centre and east of the country for SSP5-8.5, but in the north west for SSP3-7.0. This distribution per scenario is continued in Figure 9C for SSP5-8.5, but not for the other scenarios. In this timeframe SSP3-7.0 shows a focus of temperature rise across the south of the country.
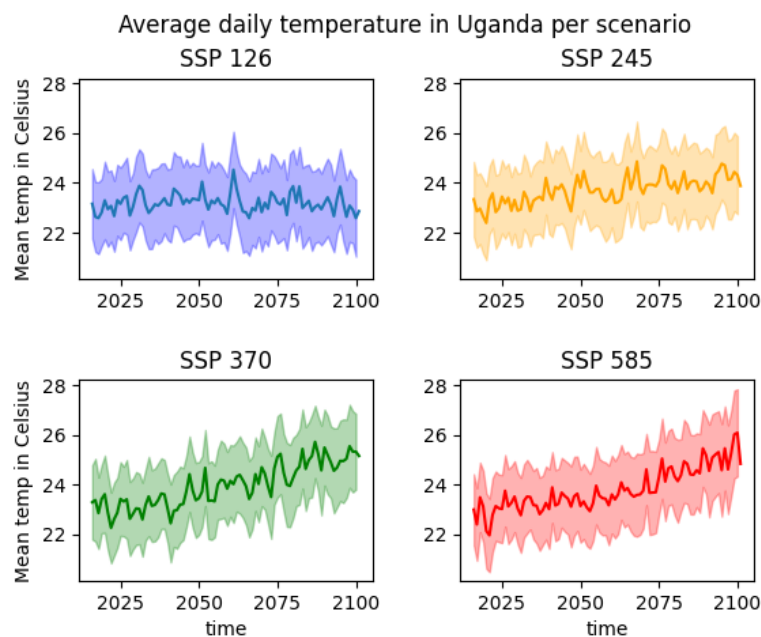

Figure 8: Average daily temperature per year in Celsius. Daily temperature values were averaged over the two spatial dimensions and resampled to a yearly mean. Lighter coloured error bands as calculated in section 4.5.1. have been added around the line of the main model.
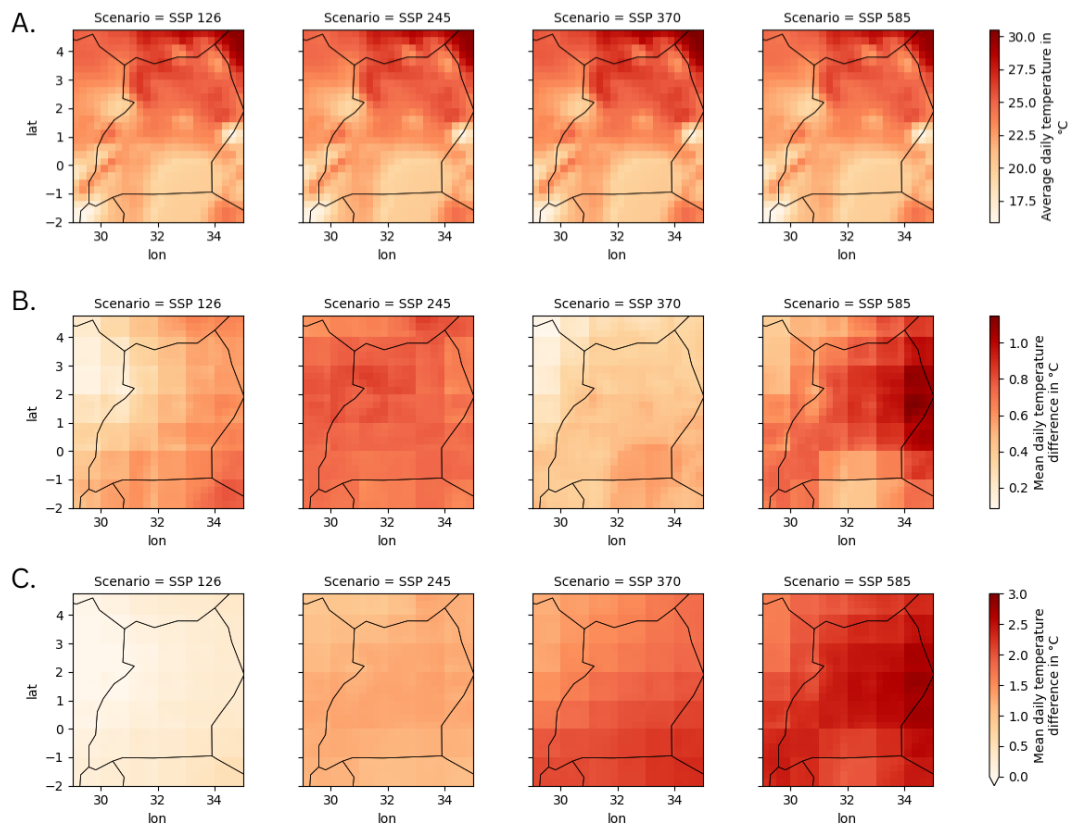
Figure 9: Average daily temperature in °C from 2015-2022 (A) and the change in °C with respect to A for the average daily temperature of time frames 2040-2060 (B) and 2080-2099 (C).

4.2. Average R_0 values

The average daily R_0 values for timeframes 2020-2040, 2050-2070 and 2080-2099 have been plotted in Figure 10. The spatial distribution of the areas that show on average a climatically suitable area for malaria transmission ($R_0 > 1$) are roughly similar across scenarios and per timeframe. It can be observed that scenarios SSP3-7.0 and SSP5-8.5 show higher R_0 values within this spatial distribution. For the same scenarios, from 2080 to 2099, an increased area for malaria transmission can be observed across the western border of Uganda. Additionally, the area of Lake Victoria in the southeast displays an average increase in R_0, becoming a suitable area for malaria transmission in the final time frame. Two cities show to be located in an area with overall high R_0 values. These are Mbale (in the East) and Kasese (in the West). Other cities that become exposed to an increased risk in the final time frame of SSP5-8.5 include Jinja, Mukono and Kira around Lake Victoria and Hoima in the Midwest of the country.
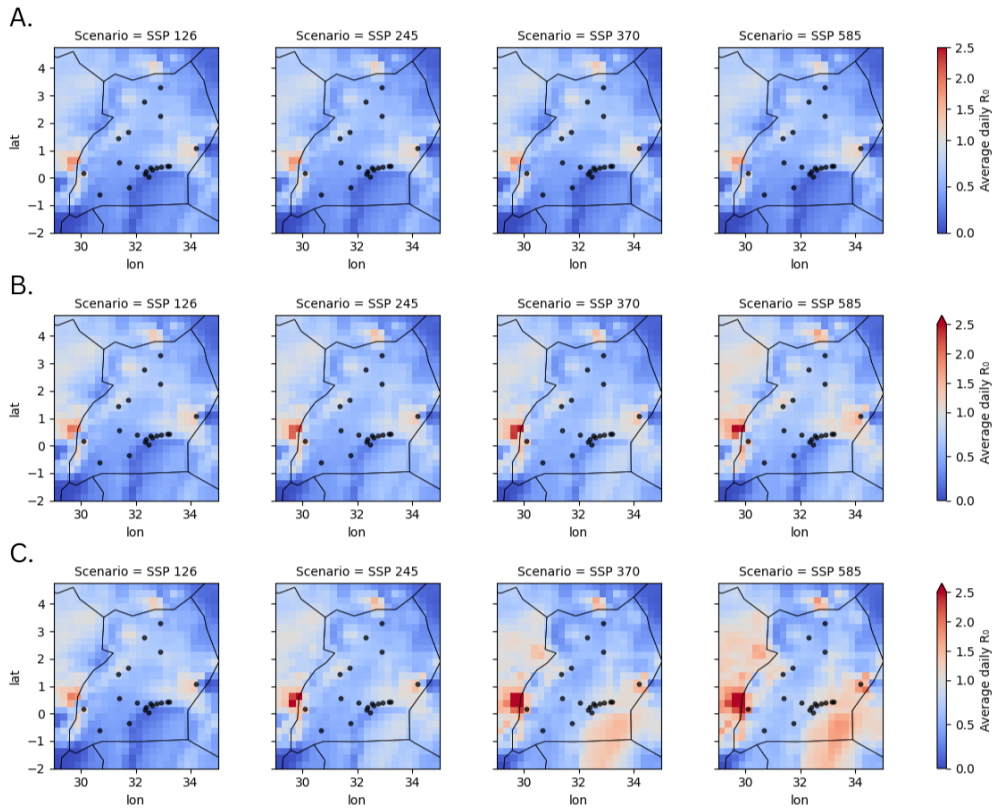
Figure 10: average daily R_0 value for time frame 2020-2040 (A), 2050-2070 (B) and 2080-2099 (C). Black dots represent the 20 major cities of Uganda (appendix A).

Table 5 shows how the proportion of land where $R_0 > 1$ increases over time, per scenario. SSP1-2.6 and SSP2-4.5 show a marginal increase, while scenario SSP3-7.0 and SSP5-8.5 display a large increase up to 34.7% of the land. Note that these values are computed over the entire study area that is displayed in the maps, thereby also including R_0 values of neighbouring areas of Uganda.

	SSP1-2.6	SSP2-4.5	SSP3-7.0	SSP5-8.5
2020-2040	3.1%	3.1%	3.2%	3.1%
2050-2070	4.3%	4.9%	6.8%	13.6%
2080-2099	4.6%	7.3%	24.1%	34.7%

Table 5: Proportion of the study area where $R_0 > 1$. For every time frame the average R_0 value was calculated per grid cell (as displayed in Figure 10). Grid cells with $R_0 > 1$ were counted and divided by the total number of grid cells in the study area

4.3. Malaria transmission season length

The malaria transmission season length is counted by computing the five-day rolling-average of R_0 and taking the subsequent counts of the days where $R_0 > 1$. To display spatial and temporal trends, the average yearly values of these counts have been plotted on the map of Uganda for each SSP scenario within the following timeframes: 2020-2040, 2050-2070, 2080-2099. The resulting plot can be seen in Figure 11. The MTS length appears to increase at later points in time (rows). Additionally, this increase appears stronger for scenarios SSP3-7.0 and SSP5-8.5. Specifically high values can be detected in the high-altitude locations in the southwest. Additionally, the region covered by Lake Victoria (southeast) also displays a relatively high increase in MTS length. Mbale and Kasese are located in areas with relatively high and over time increasing transmission seasons (up to 120 days per year). Other cities that show a notable yet smaller rise in transmission season length are Jinja, Mukono, Kira and Hoima.
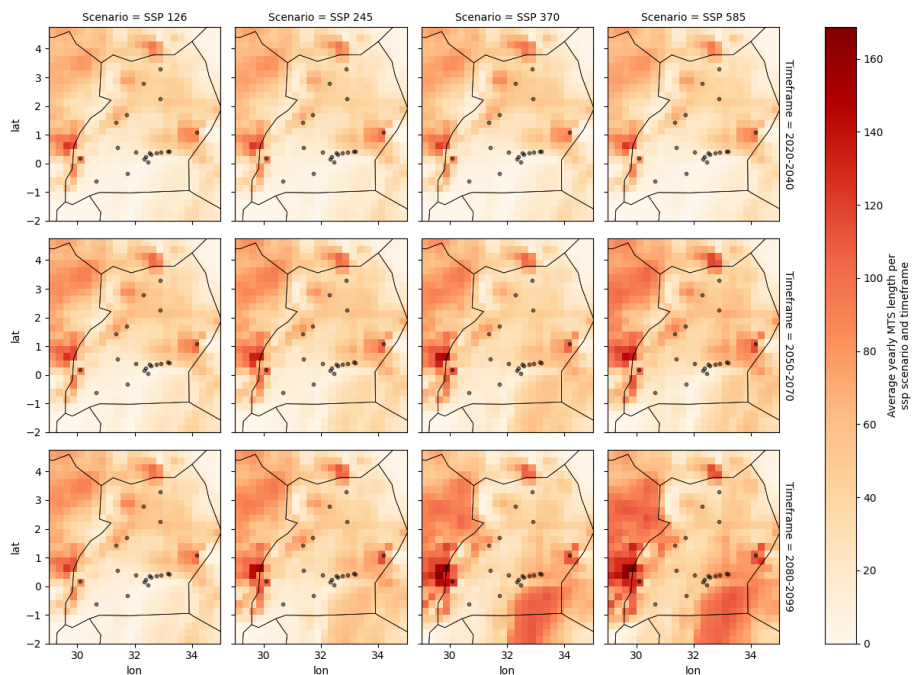
Figure 11: Average MTS length in days per year per SSP Scenario (columns) and per time frame (rows). Values are computed over the area of Uganda and averaged over time for the timeframes 2020-2040, 2050-2070, 2080-2099. Black dots represent the 20 major cities of Uganda (appendix A).

The MTS length can be further analysed by splitting the data into a spring (January to June) and fall (July to December) season. By doing so the trends per biannual rainy season can be assessed. The plots for the fall and spring seasons are visible in Figure 12A and 12B respectively. Regardless of the trends, it can be observed that the MTS is on average longer in the fall season than in the spring season. The fall season also displays a more clearly

defined trend upwards over time for scenarios SSP2-4.5, SSP3-7.0 and SSP5-8.5. Between seasons an equal amount of variation around the trend can be observed for each scenario. Between SSP scenarios, SSP3-7.0 and SSP5-8.5 show more variation around the trend than scenarios SSP1-2.6 and SSP3-7.0.
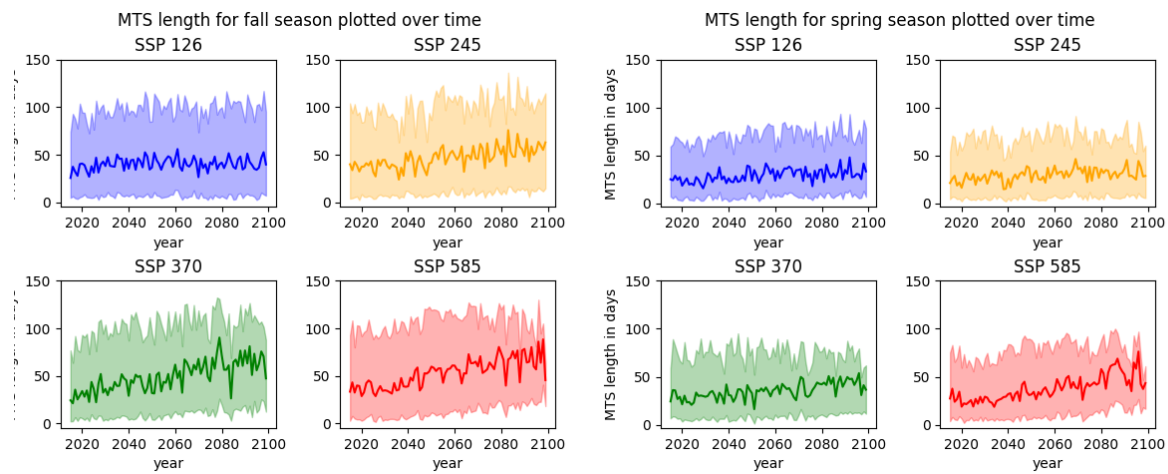

Figure 12: MTS season length for fall season and spring season. R_0 is computed for all gridcells and timesteps. Five-day rolling averages are taken to reduce daily errors. For each season the number of days where $R_0 > 1$ is counted, resulting in one count per season per gridcell. Values are averaged over the two spatial dimensions, resulting in one datapoint per season per year and plotted over time. Lighter shaded bands around the lines were created by computing R_0 for the lower and upper limit of the precipitation and temperature values.

4.4. MTS moment in time

The average moment of the MTS per season was plotted in Figure 13. Years were split into two seasons with 182 days. All days per season where the five-year rolling average of $R_0 > 1$ were recorded. The daycounts were averaged to calculate the average moment when the MTS occurs per gridcell. Values were averaged over the spatial dimensions and plotted as a five-year rolling average to assess the trends.

The spring season shows fluctuating lines that do not display a clear overall trend across scenarios. The average moment in season lies around the 110th day of the season. For the fall season the scenarios start at a lower mark, around the 100th day. Only scenario SSP5-8.5 shows a clear upward trend towards day 115. The other scenarios fluctuate more around day 100.
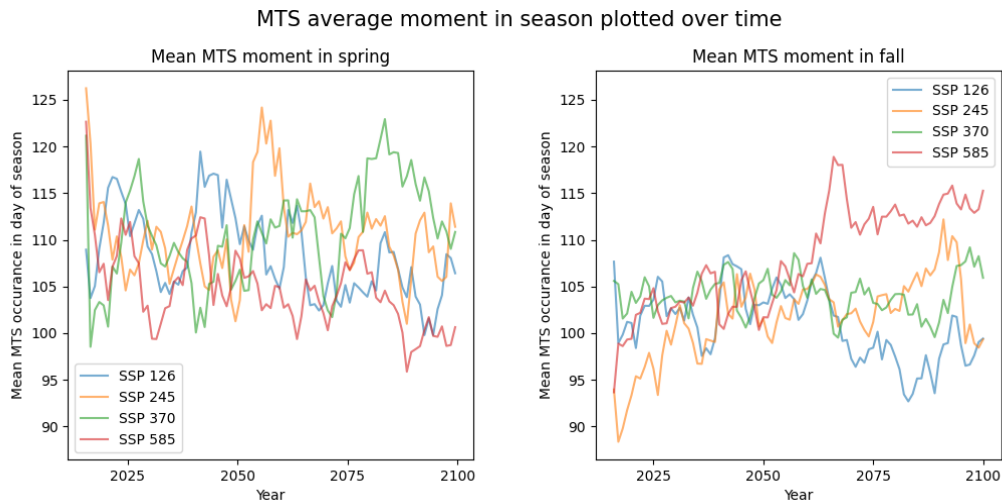
Figure 13: Average moment in season of the MTS in day of season, plotted over time for spring and fall. The day of season counts for every gridcell where $R_0 > 1$ were averaged per season. These values were averaged over the two spatial dimensions resulting in one average MTS moment per year for the spring and fall seasons.

4.5. Error analysis

4.5.1. Weather error analysis

The error bands per SSP scenario and per variable can be plotted against time to see how the error bands change per variable in the future. To facilitate trend recognition, the values were plotted as a rolling 5-year average in Figure 9.

The precipitation standard deviations show considerable variation across SSP scenarios. SSP1-2.6 and SSP2-4.5 show little variation, with the latter showing a slightly larger increasing trend than the former. SSP3-7.0 and SSP5-8.5 show considerable variation, both starting around 2.75 mm and ending around 4.0 mm. SSP5-8.5 shows a steeper trend in the first 60 years but then seems to flatten out.

The temperature standard deviations show less variation. For all scenarios the standard deviations seem to gradually increase up to the year 2085. At this point they diverge, where SSP5-8.5 displays a relatively steep increase in trend from 1.55 to 1.75.
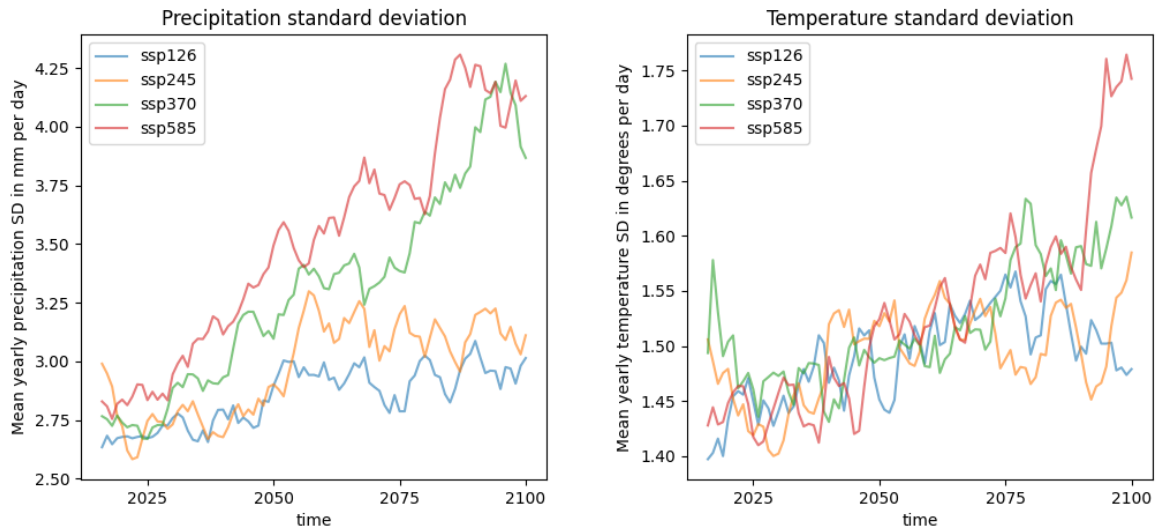
Figure 14: precipitation and temperature errors plotted over time. Standard deviations between ensemble models were computed for every timestep and gridcell. Values were averaged over the two spatial dimensions, resulting in one standard deviation per day. Values were resampled to a yearly mean and plotted as a 5-year rolling average.
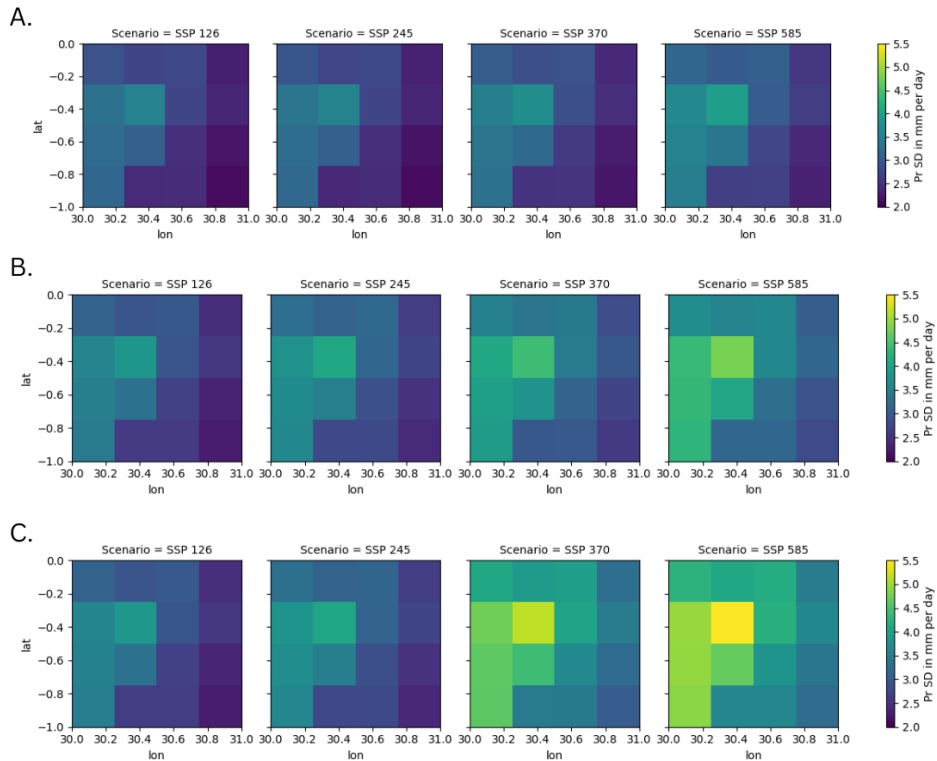
Figure 15: Spatial error distribution of precipitation values in mm day^{-1}. For each point the standard deviation across climate models was taken to estimate the error per gridcell and per timestep. The values were averaged over time for timeframes 2020-2040 (A), 2050-2070 (B) and 2080-2099 (C).

28

The spatial distribution of the precipitation error was analysed for three time frames in Figure 15: 2020-2040 (15A), 2050-2070 (15B) and 2080-2099 (15C). Note that this is the spatial distribution of the subset of the data as indicated in Figure 2 and 5. Precipitation error is highest in the midwestern region of the area, reaching values up to 5.5 mm day^{-1}. The error measures for the different scenarios all show an increase over time. This increase is relatively small for SSP1-2.6 and SSP2-4.5. The spatial distribution of the values displays a similar pattern across different scenarios and time frames.

Figure 16 displays the spatial distribution of the temperature error for three timeframes: 2020-2040 (16A), 2050-2070 (16B) and 2080-2099 (16C). The precipitation errors are highest across the north of the region, reaching values higher than 1.7°C. The values for the different scenarios all appear to increase over time, with most notable increases for SSP3-7.0 and SSP5-8.5. The spatial distribution of the values displays a similar pattern across different scenarios and time frames.
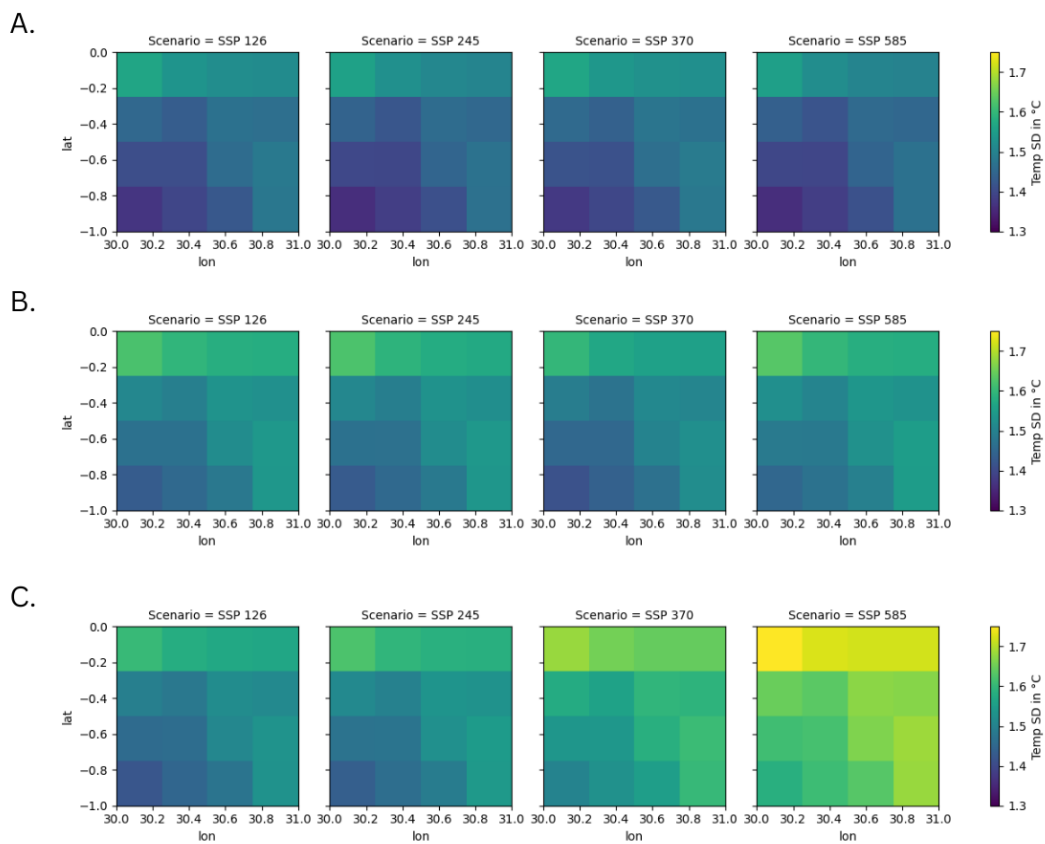

Figure 16: Spatial error distribution of temperature values in degrees Celsius per day. For each point the standard deviation across climate models was taken to estimate the error per gridcell and per timestep. The values were averaged over time for timeframes 2020-2040 (A), 2050-2070 (B) and 2080-2099 (C).

4.5.2. R_0 error analysis

The spatial distribution of the R_0 error is displayed in Figure 17. R_0 values were calculated for all possible combinations of temperature and precipitation climate models of Table 3. For every datapoint the standard deviation across these different model iterations was calculated, resulting in an error measure for every gridcell and every timestep. The values were subsequently averaged over time for time frames 2020-2040, 2050-2070 and 2080-2099. Values in the western region of the subset appear to be higher than in the east. The error margin increases over time for all scenarios, yet more intensely for scenarios SSP3-7.0 and SSP5-8.5. Values rise to a maximum of 0.6. Across scenarios, the spatial distribution shows a roughly similar pattern.
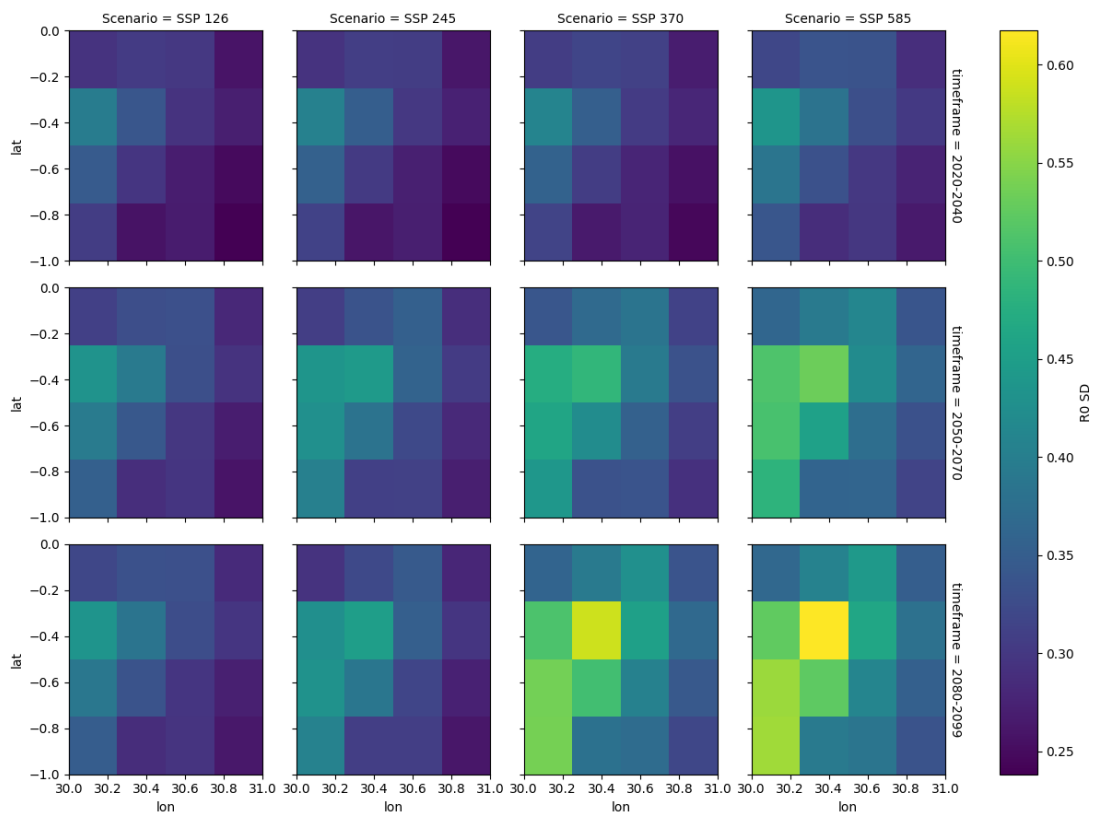
Figure 17: Spatial distribution of the R_0 error. R_0 values were calculated for all different possible combinations of climate models. The standard deviation for every datapoint was taken across these different model outputs. The standard deviations were averaged over time for the timeframes 2020-2040, 2050-2070 and 2080-2099.

4.6. Sensitivity analysis

Figure 18 displays the sensitivity curves for every parameter of the LMM_R0 model. Values were altered using the OAT method.

Sensitivity per parameter
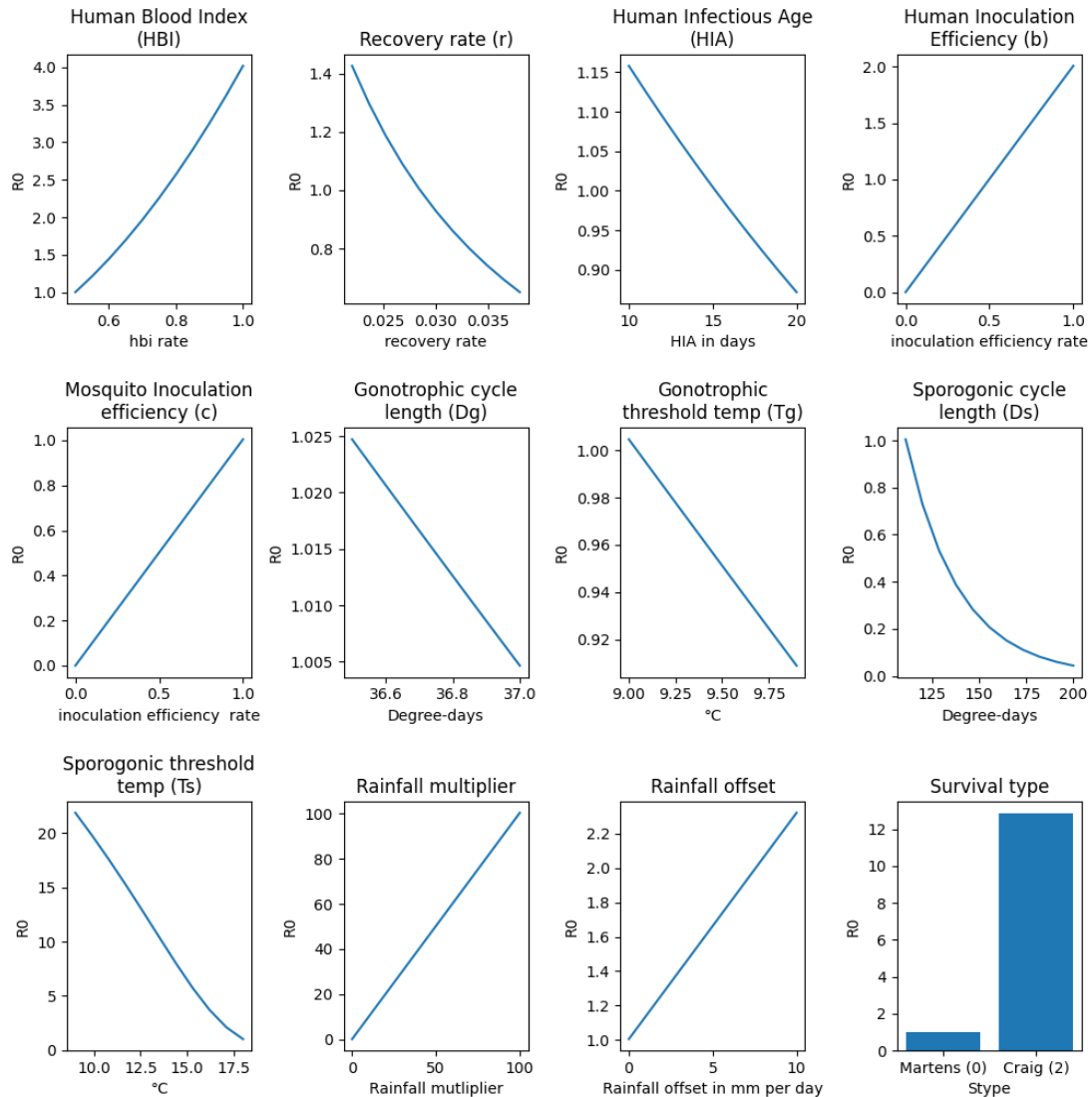
Figure 18: sensitivity per parameter setting. R_0 was calculated for a range of values per parameter for one grid cell. Values were averaged over time, resulting in one R_0 value per setting. Parameter settings and output values were plotted against each other for trend recognition.

Several parameters have a small effect on the model, partially due to the limited range of values that was tested. These are the D_g and T_g parameters. The *HIA* and *r* parameters also show a limited influence on the R_0 outcome. The parameters *c*, and D_s show a greater range of output values that is equal to 1. The parameters *HBI, T_s, b, Rainfall offset, Rainfall multiplier* and *Survival type* display a large range of output values. These parameters have a large influence on the model output. The *Rainfall multiplier* should be interpreted against the fact that the true range of possible values was unknown to Jones (2007), making it more difficult to estimate a correct range. Additionally, the high temperatures in Uganda show how

the T_s parameter can result in a huge range of output values. Decreasing the sporogonic cycle length in days (which is done by increasing the temperature, or lowering the threshold temperature) has a large effect on the output variable. A similar change can be seen for the *survival type*. The mosquito survival curve of Martens (1998) peaks around 17 degrees celsius at a survival probability of 0.9, and then decreases again to a value of 0.6 for days where the temperature is 30°C (Figure 4). The probability curve of Craig et al. (1999) decreases less quickly and maintains this maximum point of 0.9 up to a higher temperature. The high temperatures in Uganda combined with this curve cause more mosquitoes to survive to the following day. This effect accumulates up to the point where the model, on average, outputs an R_0 larger than 12.

5. Discussion

Uganda, together with the rest of the highlands of East Africa, could become more susceptible to the risk of an increased climatic suitability for malaria transmission. The relatively low temperatures at high altitudes could inhibit the spread of the disease in the present. Changes in temperature and precipitation due to climate change can cause the disease to spread further, as the spread of disease is highly weather dependent. The results section has illustrated how the spatial and temporal distribution of weather and malaria will develop under the assumptions and different SSP scenarios of the MPI climate model and the LMM_R0 model.

5.1. Climate projections

The precipitation trends show precipitation hotspots in the west, southwest and east of the country. These areas are located at relatively higher elevation levels (Figure 5). Daily rainfall in these hotspots does not increase substantially over the years for scenarios SSP1-2.6 and SSP2-4.5. For the other two scenarios, these spots show a considerable increase up to an average increase of 6mm per day from 2080 to 2099. These values should be interpreted together with the relatively wide error bands as shown in Figure 6. The spatial pattern is moderately consistent with historical patterns shown in Ngoma et al. (2021b), displaying higher rainfall for the high mountain ranges in the east and west, as well as over Lake Victoria. Overall, the MPI model predicts an increase in precipitation to various degrees. Other studies have not specifically highlighted the hotspots that were observed in the MPI output, but have assessed that Uganda can expect an increase in precipitation in the future (Onyutha et al., 2021; Ngoma et al., 2021b; Ongoma et al., 2018; Almazroui et al., 2020). Oyuntha et al. (2021), has shown that for scenarios SSP3-7.0 and SSP5-8.5 the annual

rainfall could increase with 26.3%. This has not been observed in the current study. A maximum increase in average daily precipitation of 20% could be found for the rainfall hotspot in the west of the country. Other areas in the country also show an increase in precipitation, but this increase is smaller.

The temperature values display more spatial variation in the projected changes. Temperature in the north of the country is overall highest (around 27°C), and lowest in the south (around 20°C). MPI projections show an increase in temperature for all scenarios, with more specific areas of focus depending on time frame and SSP scenario. The overall temperature increase is consistent with other studies that identified a warming trend in East Africa (Ayugi et al., 2021). Additionally the rising temperature values over the different scenarios are not fully in line with the global IPCC projections as presented in Table 1 (IPCC, 2023a). For example, the average projected temperature rise is limited to 3°C under SSP5-8.5, instead of the global projected temperature rise that is larger than 4°C. However, this was expected as Central East Africa has shown a lower temperature rise than the global temperature rise across CMIP6 models (Almazroui et al., 2020).

5.2. Malaria modelling

The meteorological trends have had the following effects on the suitability for malaria transmission. The proportion of areas where, on average, malaria is present substantially increases as time progresses for scenarios SSP3-7.0 (up to 24.1%) and SSP5-8.5 (up to 34.7%). Additionally, the seasons appear to become more intense, with higher R_0 values, especially in the areas where the rain hotspots are located. New climatically suitable areas develop on Lake Victoria for the aforementioned scenarios from 2080 to 2099.

A similar distribution of areas and intensity can be observed for the MTS length. The rain hotspot locations show a long and increasing yearly MTS up to around 140 to 160 days for SSP3-7.0 and SSP5-8.5. The rest of the country displays lower values of around 40 to 60 days per year. It appears that the MTS length increases across time for all scenarios, with SSP3-7.0 and SSP5-8.5 showing the most extreme cases. Splitting the MTS length up in the biannual rainy seasons shows longer MTS seasons during fall than during spring. The fall MTS length increases over time for scenarios SSP2-4.5, SSP3-7.0 and SSP5-8.5. This increase is largest for the latter scenario, where the MTS length increases up to 80 days on average.

The average R_0 rates and MTS length show the sensitivity of the model towards rainfall. Increased rainfall results in a high influx of new mosquitoes causing the R_0 values to spike at the rain hotspots. New areas where $R_0 > 1$ do appear, but mostly around the areas where rainfall and altitude are relatively high. A similar spatial distribution can be observed for the MTS length. In the results of both sections it appears that rainfall has a high influence on the output of the LMM_R0 model. On the contrary, the (changes in) the spatial distribution of temperature show a smaller effect on the model. It appears that the average temperatures are already high enough for creating a climatically suitable area for malaria transmission. The rainfall can then exert a larger influence on the model. These high rainfall projections appear to be correlated to the high elevation locations in Uganda. Therefore, indirectly, these high elevation levels can be related to an increase in R_0 for this study.

This observation corresponds with the research of Colón-González et al. (2021). They noted that regions in Africa located at an altitude of at least 1000 metres are more likely to have an increase in MTS length over time than regions located below this level. This trend could be observed for all six climate scenarios they tested.

Lake Victoria can potentially become a new climatically suitable area in the future. As it is a water body, and thus uninhabited, the R_0 values become harder to interpret here. It should be added that in these natural bodies of water, even if they are smaller ponds, there can exist aquatic communities containing predators that help to restrain the vector population size by eating the larvae (Roux and Robert, 2019). The LMM_R0 model does not accurately model these dynamics and might therefore overestimate R_0 values in this area.

The MTS moment in season does not show a clear trend. Values fluctuate over time between day 100 and day 120 for all scenarios in the spring season. The MTS moment in fall fluctuates less than the spring season from 2020 to 2060. Values lie approximately between day 95 and 105. Starting from 2060, SSP5-8.5 diverges from this path and shows a shift towards the end of the season (day 115). Thus, only the fall MTS moment of SSP5-8.5 moves to a later moment in the season.

There are some cities that appear to be at a particularly high risk of longer and more intense malaria transmission seasons in the future. Kasese and Mbale are located in areas that can be marked as hotspots for malaria transmission. These areas display relatively high R_0 rates at the start of the study period, but also show the highest increase over time. Both areas are subject to projected rainfall centres. It should be considered that a lot of major urban centres are located close to Lake Victoria. These cities could become more susceptible to a higher

risk of malaria at later time stages for SSP3-7.0 and SSP5-8.5. It should be noted here that the effect of urbanisation is not incorporated into the LMM_R0 model. Urbanisation has shown a negative effect on malaria transmission, reducing the mosquito biting rates and transmission intensities (Hay et al., 2005). Therefore, R_0 estimates of urban areas produced by the LMM_R0 model might be overestimated.

The findings of this study conflict to a degree with the global study that was carried out by Caminade et al. (2014). They reported an average MTS length of three or more months for the LMM_R0 model in Uganda from 2000 to 2010. Their study was inconclusive about whether this would increase or decrease. This would mean that the average yearly MTS length would be around 90 days per year. This was not observed in the output generated in this study, where most regions show an average MTS length of below 90. Furthermore, especially for SSP3-7.0 and SSP5-8.5, this study has reported an increase in MTS length over time. It should be noted that Caminade et al. (2014) computed monthly R_0 values instead of daily, complicating a proper comparison.

Caminade et al. (2014) also reported that the additional population at risk of malaria in East Africa could increase substantially over time. This could be consistent with the spread of malaria to some major urban centres in Uganda. Still, East Africa encompasses multiple countries, such as Ethiopia, where the authors noted a substantial increase in MTS length in the future. In contrast, other studies have even noted a decrease in population at risk in Uganda. By using the MIASMA model, Lieshout et al. (2004) noted a scattered decrease in population at risk of malaria for three out of four SRES emissions scenarios. Colón-Gónzalez et al. (2021) noted a decrease in MTS length in Uganda for five out of six tested climate scenarios as well. Only for scenario SSP5-8.5 they estimated an increase in Uganda.

5.3. Error and sensitivity analysis

The temperature and precipitation error bands increase over time. Projections that are further in the future show a larger uncertainty between models. This error band is especially large for the precipitation values. The average daily precipitation lies around 5mm day^{-1}, with error margins increasing up to 4.25mm day^{-1} for scenarios SSP3-7.0 and SSP5-8.5. The temperature errors are more modest, reaching from 1.4°C to 1.75°C on an average temperature that ranges from around 22°C to 26°C. The spatial distribution between the error values of the two weather phenomena are not similar. Precipitation error values are highest in the west of the ensemble region. This is approximately where the elevation levels increase (Figure 5). Still, it should be noted that elevation levels across the south are also

relatively high for the region, while the error values remain relatively low there. The temperature error values are highest in the north of the study region. This does not seem to coincide with a particular spatial distribution of the elevation levels. The error values of R_0 follow a distribution that shows a high similarity to the precipitation error distribution. High error values are observed in the western region of the area. Overall it can be seen that error values are highest for scenarios SSP3-7.0 and SSP5-8.5, particularly in the later time frames. This is consistent with the previously observed temporal trends of the meteorological phenomena. It therefore appears that uncertainty increases with time and with an increase of projected global temperature rise across SSP scenarios.

The sensitivity analysis has shown the high sensitivity of the LMM_R0 model to its parameter settings. The parameters *HBI, b, T_s, Rainfall multiplier, Rainfall offset* and *Survival type* have all shown an output range for R_0 that is larger than one. Very extreme values were found for *Survival type, Rainfall multiplier* and T_s. Other parameters, such as *c* and D_s display a range of output values that is equal to one. Overall this indicates that the model shows a low robustness towards errors in the parameter values. Studies using the model could result in disproportionate output values, if the parameter values are not accurately calibrated towards the specific situation in the study region. Additionally, it shows that the aforementioned parameters have a very high influence on the output of the model. These should be carefully considered when running the model.

The error and sensitivity analysis both indicate that R_0 values could deviate substantially for projections into the future. The R_0 error analysis displays maximum values of 0.6. Additionally, non refined parameter settings could introduce uncertainty to the R_0 estimates ranging from small output differences (D_g, T_g, *r*) to large output differences that could distort the results (*Survival type, HBI*). Together, these sources of uncertainty can introduce a large range of possible output values. Depending on which parameters are changed and the study region, R_0 values could vary by a margin of 0.3 to 4, or even 12 when considering the survival type. This warrants caution when interpreting and using the output of this model.

5.4. Limitation and research opportunities

There are several limitations to this study that need addressing. Firstly, due to limited resources it was not possible to calculate error bands that are representative of the entire study region. The choice for a spatial subset to create the ensembles, limits the error analysis to the geographical space of the ensembles. Additionally, this has led to a universal error band that was applied to every gridcell of the MPI dataset. The spatial error distribution

of the ensemble data was analysed, however this did not capture the spatial variation of the entire study region.

Secondly, a note about the data produced by the CIL is required. All the data that the CIL produced from their selection of CMIP6 models has been downscaled using the ERA5 reanalysis dataset (Hersbach et al., 2020; Sabater, 2019; Sabater, 2021). One of the known issues of the ERA5 dataset, as stated on the website of the European Centre for Medium-Range Weather Forecasts, is that it can suffer from rain bombs. Several times a year the precipitation in small areas can become extremely large, especially in regions in Africa that have a high altitude (*ERA5: Data Documentation - Copernicus Knowledge Base - ECMWF Confluence Wiki*, 2023). This is consistent with the rain hotspots that were observed for the MPI model at high-altitude locations in the east and west of the study region. Research has shown that the southwestern region of Uganda can receive enhanced rainfall in the period from June to August (Ogwang et al., 2015). Likewise, the historical analysis of Ngoma et al. (2021b) shows a similar spatial distribution of rainfall patterns as was observed in the projections. Still, the ERA5 rain bombs should be considered when interpreting the precipitation data.

Thirdly, not all sources of uncertainty have been properly addressed. As R_0 has been modelled using outputs from global climate models, there is some uncertainty that remains unspecified. This concerns the uncertainty that is generated by the projections of different greenhouse gas (GHG) emissions and their relative temperature rise as estimated by the IPCC (2023a). Within these GHG scenarios, it was noted that scenario SSP5-8.5 has become a less likely scenario (IPCC, 2023b). Therefore, any malaria projections and estimations made within this scenario should be interpreted as an extreme, improbable scenario. The uncertainty in the projections of the climate model have been addressed in the form of the calculated error bands from section 4.5.1.. Lastly there is a degree of uncertainty that is involved in the computation of R_0. This uncertainty has been addressed through a sensitivity analysis and has illustrated that the LMM_R0 model is very sensitive to its input parameters. Due to limited time and resources it was not possible to accurately calibrate the model according to observations in the study region. Instead, the parameter settings were inferred from the literature. Even though these settings were carefully considered, the R_0 values should still be interpreted with the associated uncertainty that was noted in the sensitivity analysis.

Lastly, it should be noted that the basic reproduction rate should not be compared to the prevalence of the Anopheles mosquito or the malaria incidence. It solely indicates whether

the climate is suitable for malaria transmission and with what intensity it can occur. The model is not connected to a population dataset to infer incidence rate, nor is it modelling the presence of the parasite. As Jones (2007) stated: "forecasts from such models can only really be treated as simple indicators of malaria risk". The model could become part of a more comprehensive approach to help policy makers to identify possible future malaria risks.

Future research could focus on widening the study area, encompassing (larger parts of) East Africa, and using a larger area to create ensembles for error assessment in the temperature and precipitation values. This would result in a clearer picture of the error values between datasets. Additionally, the CMIP6 project could be utilised for different types of malaria models to assess variation between model projections based on renewed climate projections. By doing so, researchers could create a sharper image of future changes in malaria distributions across Uganda and (East) Africa. Challenges for future research lie mainly in the accurate modelling of the dynamics of malaria transmission. These include, for example, the incorporation of the effects of immunity to malaria, drug resistance of the parasite and urbanisation into the model (Eikenberry & Gumel, 2018). Furthermore, additional validation research could be done to more accurately calibrate the parameter settings of the model.

6. Conclusion

The climatic conditions in Uganda appear to change in a manner that favours malaria transmission. The malaria burden of Uganda shows an increase in the upcoming decades under the assumptions of the LMM_R0 model and the MPI climate projections. Relatively high increases can be found especially under the extreme scenarios of SSP3-7.0 and SSP5-8.5. The regions with high elevation levels in the west and east of the country show high spikes in average R_0 values and in MTS length due to the high and increasing levels of precipitation modelled in these areas. Cities that can become susceptible to a higher risk of malaria include Mbale and Kasese. Likewise, the region around Lake Victoria shows to be susceptible for an increase in suitability for SSP3-7.0 and SSP5-8.5. The current research has shown that with these forcing climate scenarios a higher degree of error should be taken into account for interpretation. Furthermore, the LMM_R0 model has shown to be highly sensitive to its parameter settings, generating more uncertain estimates. More research regarding the modelling of malaria in Uganda and East Africa could help validate the results of this study, as well as generate additional output measures such as the Entomological Inoculation Rate (EIR) or the incidence rate.

7. Digital supplement

All scripts, data, licences, notices and images that were involved in the creation of this document have been shared publicly through the following link: [digital_supplement](). Note that some scripts import the data from the planetary computer. This data has already been added to the folder, but scripts have been added for reference. Further instructions on the content of the digital supplement is provided in a README file located in the supplement.

Appendix

A. Uganda cities

Largest cities in Uganda according to the 2014 census conducted by the Uganda Bureau of Statistics (Uganda Bureau of Statistics, 2016).

City	Latitude	Longitude	Population (2014 census)
Kampala	0.3136	32.5811	1,507,114
Nansana	0.3639	32.5286	365,857
Kira	0.2350	32.3820	317,428
Makindye Ssabagabo	0.1434	32.3336	282,664
Mbarara	-0.6133	30.6583	195,160
Mukono	0.3533	32.7553	162,744
Gulu	2.7817	32.2992	149,802
Lugazi	0.3833	32.9242	114,163
Masaka	-0.3411	31.7361	103,293
Kasese	0.1867	30.0881	101,557
Hoima	1.4319	31.3525	100,126
Lira	2.2472	32.9000	99,511
Mityana	0.4006	32.0422	96,075
Mubende	0.5575	31.3950	95,416
Masindi	1.6836	31.7222	94,439
Mbale	1.0806	34.1750	92,863
Jinja	0.4233	33.2039	76,057
Kitgum	3.2889	32.8778	75,594
Entebbe	0.0500	32.4600	69,430
Njeru	0.4311	33.1478	68,835
Total top 20 cities			**4,168,128**
Total population Uganda			**34,634,650**

B. Parameters of the LMM_R0 model

The parameters of the LMM_R0 model are largely similar to the settings of Kuehnert et al. (2022) and are set as follows:

Parameter	Measure	Explanation	Value	Value test range
R_{mult}	rainfall_multiplier	Rainfall to mosquito linear multiplication factor (per day)	1.0	0 to 100 (Unknown in Jones (2007)).
R_{offset}	Rainfall to mosquito offset		0.0	0 to 10 (custom)
b	Inoculation efficiency for humans	Probability of human infection given an infectious mosquito bite	0.5	0 to 1 (custom)
c	Inoculation efficiency for mosquitos	Probability of mosquito infection, when biting an infectious human	1.0	0 to 1 (custom)
HBI	Human blood index	Preference of mosquitoes to bite humans over cattle.	0.5	0.5 to 1 (Jones, 2007)
r	Human recovery rate (per day)	Rate denoting how quickly infected individuals clear infection and become susceptible again	0.0284	0.022 to 0.038 (Jones, 2007)
HIA	Human infectious age.	Number of days after infection when humans become infectious	15.0	10 to 20 days
T_g	Gonotrophic threshold temperature	Minimum threshold for the development of new larvae inside a female mosquito	9.0	9°C to 9.9°C (Jones, 2007)
D_g	Gonotrophic cycle length in degree days	Amount of degree days it takes for larvae to develop inside a female mosquito	37.0	36.5 to 37 (Jones, 2007)
T_s	Sporogonic threshold temperature	Minimum threshold for the development of the malaria parasite within the mosquito vector	18.0	9°C to 18°C
D_s	Sporogonic cycle length in degree days	Amount of degree days necessary for the malaria parasite to fully develop in the mosquito vector	111	111 - 200 degree days
$stype$	Survival type	Survival probability type: 0 = Martens (1998), 2 = Craig et al. (1999)	0	0 or 2

C.   Formulas of the LMM_R0 model

Gonotrophic cycle length in days, based on temperature *(T)* at timestep *t:*

$$G_{days,\,t} = 1 + \frac{D_g}{T_t - T_g} \tag{1}$$

Sporogonic cycle length in days, based on temperature *(T)* at timestep *t:*

$$S_{days,\,t} = 1 + \frac{D_s}{T_t - T_s} \tag{2}$$

Mosquito survival probability based on temperature *(T)* at timestep *t:*

$$P_t = 0.45 + 0.054 \cdot T_t - 0.0016 \cdot T_t^2 \tag{3}$$

Mosquito population at timestep *t,* based on the mosquito population of timestep *t-1,* the mosquito survival probability of timestep t-1 and the average daily rainfall over the previous 10 days *(R$_d$)*:

$$mos_t = mos_{t-1} \cdot P_{t-1} + R_{mult} \cdot R_d + R_{offset} \tag{4}$$

Human biting rate *(a)* at timestep *t,* denoting the number of bites on humans made by a single mosquito per day:

$$a_t = \frac{HBI}{G_{days,\,t}} \tag{5}$$

The adult mosquito mortality (μ) at timestep *t,* based on the mosquito survival probability *(P):*

$$\mu_t = -1 \cdot log(P_t) \tag{6}$$

The transmission potential at timestep *t:*

$$TP_t = \frac{a_t^2 \cdot b \cdot c \cdot exp(-\mu_t \cdot S_{days,\,t} - r \cdot HIA)}{\mu_t \cdot r} \tag{7}$$

R$_0$ at timestep *t:*

$$R_{0,\,t} = mos_t \cdot TP_t \tag{8}$$

References

Almazroui, M., Saeed, F., Saeed, S., Nazrul Islam, M., Ismail, M., Klutse, N. A. B., & Siddiqui, M. H. (2020). Projected change in temperature and precipitation over Africa from CMIP6. *Earth Systems and Environment*, *4*, 455-475. https://doi.org/10.1007/s41748-020-00161-x

Antinori, S., Galimberti, L., Milazzo, L., & Corbellino, M. (2012). Biology of human malaria plasmodia including Plasmodium knowlesi. *Mediterranean journal of hematology and infectious diseases*, *4*(1). https://doi.org/10.4084/MJHID.2012.013

Ayugi, B., Ngoma, H., Babaousmail, H., Karim, R., Iyakaremye, V., Sian, K. T. L. K., & Ongoma, V. (2021). Evaluation and projection of mean surface temperature using CMIP6 models over East Africa. Journal of African Earth Sciences, 181, 104226. https://doi.org/10.1016/j.jafrearsci.2021.104226

Ayugi, B., Zhihong, J., Zhu, H., Ngoma, H., Babaousmail, H., Rizwan, K., & Dike, V. (2021b). Comparison of CMIP6 and CMIP5 models in simulating mean and extreme precipitation over East Africa. *International Journal of Climatology*, *41*(15), 6474-6496. https://doi.org/10.1002/joc.7207

Babaousmail, H., Ayugi, B. O., Ojara, M., Ngoma, H., Oduro, C., Mumo, R., & Ongoma, V. (2023). Evaluation of CMIP6 models for simulations of diurnal temperature range over Africa. *Journal of African Earth Sciences*, *202*, 104944. https://doi.org/10.1016/j.jafrearsci.2023.104944

Bentsen, M., Oliviè, D. J. L., Seland, Ø., Toniazzo, T., Gjermundsen, A., Graff, L. S., … Schulz, M. (2019a). *NCC NorESM2-MM model output prepared for CMIP6 CMIP*. Version 20191108. Earth System Grid Federation. https://doi.org/10.22033/ESGF/CMIP6.506

Bentsen, M., Oliviè, D. J. L., Seland, Ø., Toniazzo, T., Gjermundsen, A., Graff, L. S., … Schulz, M. (2019b). *NCC NorESM2-MM model output prepared for CMIP6 ScenarioMIP*. Version 20191108. Earth System Grid Federation. https://doi.org/10.22033/ESGF/CMIP6.608

Caminade, C., Kovats, S., Rocklov, J., Tompkins, A. M., Morse, A. P., Colón-González, F. J.,
... & Lloyd, S. J. (2014). Impact of climate change on global malaria distribution.
Proceedings of the National Academy of Sciences, *111*(9), 3286-3291.
https://doi.org/10.1073/pnas.130208911

Colón-González, F. J., Sewe, M. O., Tompkins, A. M., Sjödin, H., Casallas, A., Rocklöv, J., ...
& Lowe, R. (2021). Projecting the risk of mosquito-borne diseases in a warmer and
more populated world: a multi-model, multi-scenario intercomparison modelling
study. *The Lancet Planetary Health*, *5*(7), e404-e414.
https://doi.org/10.1016/S2542-5196(21)00132-7

Craig, M. H., Snow, R. W., & le Sueur, D. (1999). A climate-based distribution model of
malaria transmission in sub-Saharan Africa. Parasitology today, 15(3), 105-111.
https://doi.org/10.1016/S0169-4758(99)01396-4

Detinova, T. S., Bertram, D. S., & World Health Organization. (1962). *Age-grouping methods
in Diptera of medical importance, with special reference to some vectors of malaria*.
World Health Organization. Retrieved from:
https://apps.who.int/iris/bitstream/handle/10665/41724/WHO_MONO_47_(part1).pdf

EC-Earth Consortium (EC-Earth) (2019). *EC-Earth-Consortium EC-Earth3 model output
prepared for CMIP6 CMIP*. Version 20200310. Earth System Grid Federation.
https://doi.org/10.22033/ESGF/CMIP6.181

EC-Earth Consortium (EC-Earth) (2019b). *EC-Earth-Consortium EC-Earth3 model output
prepared for CMIP6 ScenarioMIP*. Version 20200310. Earth System Grid Federation.
https://doi.org/10.22033/ESGF/CMIP6.251

EC-Earth Consortium (EC-Earth) (2019c). *EC-Earth-Consortium EC-Earth3-Veg model
output prepared for CMIP6 CMIP*. Version 20200225. Earth System Grid Federation.
https://doi.org/10.22033/ESGF/CMIP6.642

EC-Earth Consortium (EC-Earth) (2019d). *EC-Earth-Consortium EC-Earth3-Veg model
output prepared for CMIP6 ScenarioMIP*. Version 20200225. Earth System Grid
Federation. https://doi.org/10.22033/ESGF/CMIP6.727

Eikenberry, S. E., & Gumel, A. B. (2018). Mathematical modeling of climate change and malaria transmission dynamics: a historical review. *Journal of mathematical biology*, *77*, 857-933. https://doi.org/10.1007/s00285-018-1229-7

ERA5: data documentation - Copernicus Knowledge Base - ECMWF Confluence Wiki. (2023, June 2). https://confluence.ecmwf.int/display/CKB/ERA5%3A+data+documentation

European Space Agency, Sinergise (2021). *Copernicus Global Digital Elevation Model*. Distributed by OpenTopography. Accessed: 2023-06-21. https://doi.org/10.5069/G9028PQB

Eyring, V., Bony, S., Meehl, G. A., Senior, C. A., Stevens, B., Stouffer, R. J., & Taylor, K. E. (2016). Overview of the Coupled Model Intercomparison Project Phase 6 (CMIP6) experimental design and organization. *Geoscientific Model Development*, *9*(5), 1937-1958. https://doi.org/10.5194/gmd-9-1937-2016

Gergel, D. R., Malevich, S. B., McCusker, K. E., Tenezakis, E., Delgado, M. T., Fish, M. A., and Kopp, R. E. (2023). Global downscaled projections for climate impacts research (GDPCIR): preserving extremes for modeling future climate impacts, *EGUsphere* [preprint]. https://doi.org/10.5194/egusphere-2022-1513

Gergel, D., McCusker, K., Malevich, B., Tenezakis, E., Fish, M., Delgado, M. (2022). ClimateImpactLab/downscaleCMIP6: (v1.0.0). Zenodo. https://doi.org/10.5281/zenodo.6403794

Good, P., Sellar, A., Tang, Y., Rumbold, S., Ellis, R., Kelley, D., Kuhlbrodt, T., Walton, J. (2019). *MOHC UKESM1.0-LL model output prepared for CMIP6 ScenarioMIP*. SSP1-2.6 version 20190708; SSP2-4.5 version 20190715; SSP3-7.0 version 20190726; SSP5-8.5 version 20190726. Earth System Grid Federation. https://doi.org/10.22033/ESGF/CMIP6.1567

Hay, S. I., Rogers, D. J., Randolph, S. E., Stern, D. I., Cox, J., Shanks, G. D., & Snow, R. W. (2002). Hot topic or hot air? Climate change and malaria resurgence in East African highlands. *Trends in parasitology*, *18*(12), 530-534. https://doi.org/10.1016/S1471-4922(02)02374-7

Hay, S. I., Guerra, C. A., Tatem, A. J., Atkinson, P. M., & Snow, R. W. (2005). Urbanization, malaria transmission and disease burden in Africa. *Nature Reviews Microbiology*, *3*(1), 81-90. https://doi.org/10.1038/nrmicro1069

Hersbach, H., Bell, B., Berrisford, P., Hirahara, S., Horányi, A., Muñoz-Sabater, J., ... & Thépaut, J. N. (2020). The ERA5 global reanalysis. *Quarterly Journal of the Royal Meteorological Society*, *146*(730), 1999-2049. https://doi.org/10.1002/qj.3803

Hoshen, M. B., & Morse, A. P. (2004). A weather-driven model of malaria transmission. *Malaria journal*, *3*, 1-14. https://doi.org/10.1186/1475-2875-3-32

IPCC (2023a). *Summary for Policymakers.* In: *Climate Change 2023: Synthesis Report. A Report of the Intergovernmental Panel on Climate Change*. Contribution of Working Groups I, II and III to the Sixth Assessment Report of the Intergovernmental Panel on Climate Change [Core Writing Team, H. Lee and J. Romero (eds.)]. IPCC, Geneva, Switzerland, 36 pages. (in press). Retrieved from: https://www.ipcc.ch/report/ar6/syr/

IPCC (2023b). *Longer report.* In: *Climate Change 2023: Synthesis Report. A Report of the Intergovernmental Panel on Climate Change*. Contribution of Working Groups I, II and III to the Sixth Assessment Report of the Intergovernmental Panel on Climate Change. IPCC, Geneva, Switzerland, 85 pages. (in press). Retrieved from: https://www.ipcc.ch/report/ar6/syr/

John, J. G., Blanton, C., McHugh, C., Radhakrishnan, A., Rand, K., Vahlenkamp, H., … Zeng, Y. (2018). *NOAA-GFDL GFDL-ESM4 model output prepared for CMIP6 ScenarioMIP*. Version 20180701. Earth System Grid Federation. https://doi.org/10.22033/ESGF/CMIP6.1414

Jones, A. E. (2007). *Seasonal ensemble prediction of malaria in Africa* (Doctoral dissertation, University of Liverpool). Retrieved from: https://ethos.bl.uk/OrderDetails.do?uin=uk.bl.ethos.479049

Krasting, J. P., John, J., Blanton, C., McHugh, C., Nikonov, S., Radhakrishnan, A., … Zhao, M. (2018). *NOAA-GFDL GFDL-ESM4 model output prepared for CMIP6 CMIP*. Version 20190726. Earth System Grid Federation. https://doi.org/10.22033/ESGF/CMIP6.1407

Kuehnert, J. (2022). A Surrogate Model Benchmark for Dynamic Climate Impact Models. *IBM/UQ-climate-impact-benchmarking*. https://github.com/IBM/UQ-climate-impact-benchmarking/tree/main

Kuehnert, J., McGlynn, D., Remy, S. L., Walcott-Bryant, A., & Jones, A. (2022). Surrogate Ensemble Forecasting for Dynamic Climate Impact Models. *arXiv preprint arXiv:2204.05795*. https://doi.org/10.48550/arXiv.2204.05795

Li, L. (2019). *CAS FGOALS-g3 model output prepared for CMIP6 CMIP*. Version 20190826.Earth System Grid Federation. https://doi.org/10.22033/ESGF/CMIP6.1783

Li, L. (2019b). *CAS FGOALS-g3 model output prepared for CMIP6 ScenarioMIP.* SSP1-2.6 version 20190818; SSP2-4.5 version 20190818; SSP3-7.0 version 20190820; SSP5-8.5 tasmax version 20190819; SSP5-8.5 tasmin version 20190819; SSP5-8.5 pr version 20190818. Earth System Grid Federation. https://doi.org/10.22033/ESGF/CMIP6.2056

Lieshout, M. van, Kovats, R. S., Livermore, M. T. J., & Martens, P. (2004). Climate change and malaria: analysis of the SRES climate and socio-economic scenarios. *Global environmental change*, *14*(1), 87-99. https://doi.org/10.1016/j.gloenvcha.2003.10.009

Martens, W. J. (1998). Health impacts of climate change and ozone depletion: an ecoepidemiologic modeling approach. *Environmental health perspectives*, *106*(suppl 1), 241-251. https://doi.org/10.1289/ehp.98106s1241

MalaRis. (n.d.). http://www.impetus.uni-koeln.de/malaris/lmm_en.html

Microsoft Planetary Computer. (n.d.). https://planetarycomputer.microsoft.com/dataset/cil-gdpcir-cc0

Mordecai, E. A., Ryan, S. J., Caldwell, J. M., Shah, M. M., & LaBeaud, A. D. (2020). Climate change could shift disease burden from malaria to arboviruses in Africa. *The Lancet Planetary Health*, *4*(9), e416-e423. https://doi.org/10.1016/S2542-5196(20)30178-9

Muñoz Sabater, J. (2019). ERA5-Land hourly data from 1981 to present. *Copernicus Climate Change Service (C3S) Climate Data Store (CDS)*, *10*(10.24381). https://doi.org/10.24381/cds.68d2bb30

Muñoz Sabater, J., (2021). ERA5-Land hourly data from 1950 to 1980. *Copernicus Climate Change Service (C3S) Climate Data Store (CDS)*. Accessed: 21-05-2021. https://doi.org/10.24381/cds.e2161bac

Ngoma, H., Wen, W., Ayugi, B., Babaousmail, H., Karim, R., & Ongoma, V. (2021a). Evaluation of precipitation simulations in CMIP6 models over Uganda. *International Journal of Climatology*, *41*(9), 4743-4768. https://doi.org/10.1002/joc.7098

Ngoma, H., Wen, W., Ojara, M., & Ayugi, B. (2021b). Assessing current and future spatiotemporal precipitation variability and trends over Uganda, East Africa, based on CHIRPS and regional climate model datasets. *Meteorology and Atmospheric Physics*, *133*, 823-843. https://doi.org/10.1007/s00703-021-00784-3

Ngoma, H., Ayugi, B., Onyutha, C., Babaousmail, H., Lim Kam Sian, K. T., Iyakaremye, V., ... & Ongoma, V. (2022). Projected changes in rainfall over Uganda based on CMIP6 models. *Theoretical and Applied Climatology*, *149*(3-4), 1117-1134. https://doi.org/10.1007/s00704-022-04106-4

Ongoma, V., Chen, H., & Gao, C. (2018). Projected changes in mean rainfall and temperature over East Africa based on CMIP5 models. *International Journal of Climatology*, *38*(3), 1375-1392. https://doi.org/10.1002/joc.5252

Ogwang, B. A., Chen, H., Tan, G., Ongoma, V., & Ntwali, D. (2015). Diagnosis of East African climate and the circulation mechanisms associated with extreme wet and dry events: a study based on RegCM4. *Arabian Journal of Geosciences*, *8*, 10255-10265. https://doi.org/10.1007/s12517-015-1949-6

Onyutha, C., Asiimwe, A., Ayugi, B., Ngoma, H., Ongoma, V., & Tabari, H. (2021). Observed and future precipitation and evapotranspiration in water management zones of Uganda: CMIP6 projections. *Atmosphere*, *12*(7), 887. https://doi.org/10.3390/atmos12070887

Ototo, E. N., Ogutu, J. O., Githeko, A., Said, M. Y., Kamau, L., Namanya, D., ... & Mutimba, S. (2022). Forecasting the Potential Effects of Climate Change on Malaria in the Lake Victoria Basin Using Regionalized Climate Projections. *Acta Parasitologica*, 1-29. https://doi.org/10.1007/s11686-022-00588-4

Palmer, P. I., Wainwright, C. M., Dong, B., Maidment, R. I., Wheeler, K. G., Gedney, N., ... & Turner, A. G. (2023). Drivers and impacts of Eastern African rainfall variability. *Nature Reviews Earth & Environment*, 1-17. https://doi.org/10.1038/s43017-023-00397-x

Pascual, M., Ahumada, J. A., Chaves, L. F., Rodo, X., & Bouma, M. (2006). Malaria resurgence in the East African highlands: temperature trends revisited. *Proceedings of the National Academy of Sciences*, *103*(15), 5829-5834. https://doi.org/10.1073/pnas.0508929103

Roux, O., & Robert, V. (2019). Larval predation in malaria vectors and its potential implication in malaria transmission: an overlooked ecosystem service?. *Parasites & vectors*, *12*, 1-11. https://doi.org/10.1186/s13071-019-3479-7

Riahi, K., Van Vuuren, D. P., Kriegler, E., Edmonds, J., O'neill, B. C., Fujimori, S., ... & Tavoni, M. (2017). The Shared Socioeconomic Pathways and their energy, land use, and greenhouse gas emissions implications: An overview. *Global environmental change*, *42*, 153-168. https://doi.org/10.1016/j.gloenvcha.2016.05.009

Smith, D. L., McKenzie, F. E., Snow, R. W., & Hay, S. I. (2007). Revisiting the basic reproductive number for malaria and its implications for malaria control. *PLoS biology*, *5*(3), e42. https://doi.org/10.1371/journal.pbio.0050042

Swart, N. C., Cole, J. N. S., Kharin, V. V., Lazare, M., Scinocca, J. F., Gillett, N. P., … Sigmond, M. (2019a). *CCCma CanESM5 model output prepared for CMIP6 CMIP*. Version 20190429. Earth System Grid Federation. https://doi.org/10.22033/ESGF/CMIP6.1303

Swart, N. C., Cole, J. N. S., Kharin, V. V., Lazare, M., Scinocca, J. F., Gillett, N. P., … Sigmond, M. (2019b). *CCCma CanESM5 model output prepared for CMIP6 ScenarioMIP*. Version 20190429. Earth System Grid Federation. https://doi.org/10.22033/ESGF/CMIP6.1317

Tang, Y., Rumbold, S., Ellis, R., Kelley, D., Mulcahy, J., Sellar, A., Walton, J., Jones, C. (2019). *MOHC UKESM1.0-LL model output prepared for CMIP6 CMIP*. Version 20190627. Earth System Grid Federation. https://doi.org/10.22033/ESGF/CMIP6.1569

Uganda Bureau of Statistics. (2016). *The National Population and Housing Census 2014 – Main Report*. Retrieved from: https://www.ubos.org/wp-content/uploads/publications/03_20182014_National_Census_Main_Report.pdf

Wieners, K., Giorgetta, M., Jungclaus, J., Reick, C., Esch, M., Bittner, … Roeckner, E. (2019a). *MPI-M MPIESM1.2-LR model output prepared for CMIP6 CMIP*. Version *20190710*. Earth System Grid Federation. https://doi.org/10.22033/ESGF/CMIP6.742

Wieners, K., Giorgetta, M., Jungclaus, J., Reick, C., Esch, M., Bittner, … Roeckner, E. (2019b). *MPI-M MPIESM1.2-LR model output prepared for CMIP6 ScenarioMIP.* Version 20190710. Earth System Grid Federation. https://doi.org/10.22033/ESGF/CMIP6.793

Woldemeskel, F. M., Sharma, A., Sivakumar, B., & Mehrotra, R. (2012). An error estimation method for precipitation and temperature projections for future climates. *Journal of Geophysical Research: Atmospheres*, *117*(D22). https://doi.org/10.1029/2012JD018062

Xin, X., Zhang J., Zhang, F., Wu, T., Shi, X., Li, J., … Wei, M. (2018). *BCC BCC-CSM2MR model output prepared for CMIP6 CMIP*. Version 20181126. Earth System Grid Federation. https://doi.org/10.22033/ESGF/CMIP6.1725

Xin, X., Wu, T., Shi, X., Zhang, F., Li, J., Chu, M., … Wei, M. (2019). *BCC BCC-CSM2MR model output prepared for CMIP6 ScenarioMIP*. SSP1-2.6 version 20190315; SSP2-4.5 version 20190318; SSP3-7.0 version 20190318; SSP5-8.5 version 20190318. Earth System Grid Federation. https://doi.org/10.22033/ESGF/CMIP6.1732